Technoarete Transactions on Electrical Vehicles and Automotive systems

Volume No. 4

Issue No. 3

SEPTEMBER - DECEMBER 2025

ENRICHED PUBLICATIONS PVT.LTD

JE - 18,Gupta Colony, Khirki Extn,
Malviya Nagar, New Delhi - 110017.
E- Mail: info@enrichedpublication.com
Phone :- +91-8877340707

Technoarete Transactions on Electrical Vehicles and Automotive systems

Aim & Scope

Technoarete Transactions on Advances in Electric Vehicles and Automotive Systems (TTAEVAS) is a double-blinded Peer-reviewed open access International Journal published by Technoarete Publishing. This journal aims to cover research studies pertaining to electric cars, hydrogen fluid cells, in-vehicle production of electricity, electronics for electric vehicles, automatic components, electrical machine for automatic propulsion, "zero-emission" range vehicles, electromagnetic research issue of electric vehicles, energy management technique and strategies, super capacitors, electric motors, control system design for electric vehicles, charging mechanisms of electric vehicles, electric trains, electric ships, electric aircrafts, electrification of heavy- duty vehicles, hybrid electric vehicles, electrification of off-road vehicles, sustainable energy systems, intelligent transportation system for vehicle, environmental impact of electric vehicles, fuel cell vehicles, heavy duty buses, battery management system, electric air conditioner mechanism for electric vehicles, sensor and propulsion system, stability analysis and vehicle Motion Control heating system for electric vehicles power semiconductor devices, wide bandgap devices, seasons for electric motors and converters wireless power transfer mechanism for electric vehicles.

Technoarete Transactions on Electrical Vehicles and Automotive systems

(Volume No. 4, Issue No. 3 , SEP - DEC 2025)

Contents

Computational Flow Analysis of Carburetor Venturi Effecting On Obstacles

Ivarayudu, Dr. B.[2] Jayachandraiah ,
PG scholar, Department of Mechanical[1] Engineering, SKIT/JNTUA, India
Professor, Department of Mechanical[2] Engineering, SKIT/JNTUA, India

A B S T R A C T

A computational fluid dynamics (CFD) is used to develop a three dimensional, fully turbulent model of the compressible flow across a complex-geometry venturi, such as those typically found in small engine carburetors. An attempt is made in this paper to carry- out three dimensional CFD analysis of effecting on carburetor venturi with obstacles and fuel tube to draw various types' contours of the static pressure, velocity, total pressure and turbulent kinetic energy. First is to model the carburetor venture using CFD tool and meshed by volume mesh with 84, 605 Tetrahedron elements. Then the CFD analysis is carried–out and presented results, is observed result drawn for various types of static pressure, velocity, total pressure and turbulent kinetic energy is effecting the fuel tube and venturi without obstacles and effecting on modified obstacles, It is observed that the obstacles located at converging nozzle of the venturi do not cause significant pressure losses, while those obstacles wakes on the flow. Significantly, once the mass flow rate is corrected using an overall discharge coefficient, the knowledge of the actual Cross-sectional area at the venturi throat is enough to calculate the static pressure and Stagnation Pressure(total pressure) at the tip of the fuel tube. The evaluated results are validated with mathematical model, its good agreement.

Keywords: CFD, carburetor, venturi

INTRODUCTION

Carburetor: The carburetor is a device that mixes fuel into the incoming air. The airflow into the carburetor is controlled by a butterfly valve, and the fuel is added to the mixture through venturi. In a carburetor equipped engine. The air comes in to the space for air filter. Air passes through the air filter and then into the carburetor where the fuel is blended with it. Through the intake manifold, it passes. And then it is drawn into the cylinders.

Large volumes of small engines (two wheelers) are being sold in India every year. Its emissions comprise a significant percentage of total pollutants in India. As demonstrated by the automotive industry, significant reductions in emissions are technologically possible, particularly with the use of electronic fuel injection. However, due primarily to cost constraints, small engine manufacturers rely on small, inexpensive Carburetors to generate the fuel mixture for their engines. Thus, a better understanding of carburetor performance and modeling could lead to better fuel mixture control and lower emission

From small engines

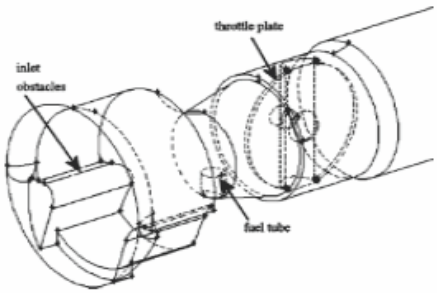

Fig 1: Details of carburetor parts inside the venturi

A real carburetor venturi has details in its geometry that create disturbances in the flow and may cause pressure losses that cause deviations from an ideal isentropic flow. These carburetor parts are the choke plate, throttle plate, fuel tube, side passages to secondary systems, and, sometimes, an additional concentric fuel tube in the venturi throat. Some details of typical carburetors used in small engines are shown in above figure1.

LITERATURE REVIEW

This Literature review section provides an insight into the research in the present paper the inlet obstacles, fuel tube, and throttle plate were modeled with in order to gain a better understanding of the flow in complex venturis. Several studies have addressed the modeling of fuel flow in carburetors: Experimental studies performed by Furuyama and Ohgane [1] and Moss [2] showed that the pulsating nature of the air flow affects the amount of fuel delivered by the carburetor. Furuyama found that the effect of pulsating air flow on fuel flow may be classified as: i) when the throttle plate opening is large and air flow is low, the fuel flow is higher at pulsating flow than at steady flow, and ii) when the throttle plate opening is large and air flow is high, the fuel flow is lower at pulsating flow than at steady flow. Moss' experiments [1] agreed with the conclusions for the first case. Both researchers proposed that the fuel flow under dynamic air flow may be calculated by using the steady state prediction, and then corrected with a pulsation- correction factor. Two special considerations must be taken when predicting the fuel flow from the carburetor circuits: the characterization of the two-phase flow inside the emulsion tube and the characterization of the small metering orifices.

The only known work that has used CFD for the characterization of the flow across the carburetor was done by Wu, Feng and Liu [3]. But in their work, the carburetor was represented as a two-dimensional channel where the fuel tube was a large obstacle in the flow field. The only results shown in this work are the static pressure drop along the axis of the carburetor.

Thus, it can be inferred from these works that the flow through a carburetor can be successfully modeled using pressure variation as boundary conditions and the standardized k-epsilon turbulence model is competent enough to model the turbulence behavior in the flow.

OBJECTIVE OF THE PAPER

To carry out three dimensional CFD analysis of carburetor venturi to understand the effect of the various obstacles present in the flow domain like the fuel-tube, throttle plate and to optimize the design of carburetor by carrying out geometrical changes based on results obtained from CFD analysis of existing model.

- To perform CFD analysis by considering the following models.

a) Ideal carburetor venturi
b) Existing carburetor venturi
c) Modified carburetor venturi

MODELING INTRODUCTION

Basic steps of modeling:

Stage 1: preprocessing

Geometry definition: the physical boundaries of the objects are defined in a 3-dimensional space.

Meshing: the volume bound by the body or the fluid domain is discretised into finite elements that are uniform or Non-uniform as the problem demands.

Model definition: the type of fluid modeling is defined in terms of the flow equations adopted or the energy Transfer models etc.

Boundary conditions: the boundary or end conditions of the flow are defined in the software module The inlet boundary condition was defined with the isentropic stagnation pressure and temperature, and the outlet boundary condition was defined with the outlet static pressure. An ideal gas model was used in order to take into account the compressibility of the airflow.

Method

A three-dimensional model of a carburetor venturi was generated in CFD tool, The model build option crate line and create surface, by using extrude surface and then we create that venture geometry, this model saved In IGS for met and then it is export to using ICM software for meshing and element type Tetrahedron the mesh is created. This file is saved in *mesh for met and it is used CFX for CFD analysis.

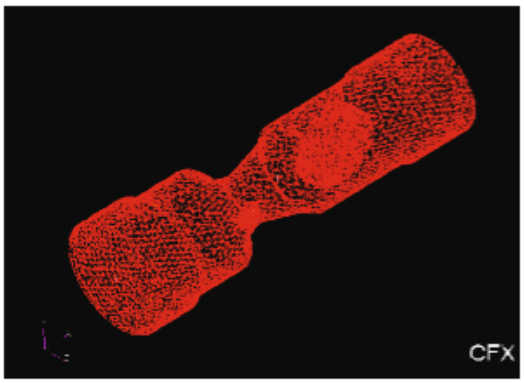

Fig 2. Meshed model

Meshing Model Details:

Element type	: Tetrahedron
Global Element Scale Factor	: 4.3
Mesh Type	: Volume mesh
No. of elements	: 84,605

Mathematical Modelling

Air is used as fluid media, which is assumed to be steady and incompressible. High Reynolds number k-ε turbulence model was used in the CFD model. This turbulence model is widely used in industrial applications. The equations of mass and momentum were solved using SIMPLE algorithm to get velocity and pressure in the fluid domain. The assumption of an isotropic turbulence field used in this turbulence model was valid for the current application. The near-wall cell thickness was calculated to satisfy the logarithmic law of the wall boundary. Other fluid properties were taken as constants. Filter media of intake system and air sensor were modeled as porous media using coefficients.

For porous media, it is assumed that, within the volume containing the distributed resistance there exists a local balance everywhere between pressure and resistance forces such that

$$-K_i u_i = \frac{\partial p}{\partial \xi}$$

Where ξ_i (i = 1, 2, 3) represents the (mutually orthogonal) orthotropic directions.

K_i is the permeability

u_i is the superficial velocity in direction ξ_i

The permeability K_i is assumed to be a quasi linear function of the superficial velocity magnitude of the form

$$\alpha_i \left|\vec{v}\right| + \beta_i$$

Where α_i and β_i are user-defined coefficients

Superficial velocity at any cross section through the porous medium is defined as the volume flow rate divided by the total cross sectional area (i.e. area occupied by both fluid and solid). In this analysis, α_i and β_i are assumed to be same.

ANALASIS INTRODUCTION

CFD : Computational fluid dynamics (CFD) is one of the branches of fluid mechanics that uses numerical methods and algorithms to solve and analyze problems that involve fluid flows. Until 1960's we would have been operating in “two approach world” theory and experiment. Later an important new third approach in fluid dynamics is introduced.

The ANSYS CFX : solver uses the most modern solution technology with a coupled algebraic multi-grid solver and extremely efficient parallelization to help ensure that solutions are ready for analysis quickly and reliably. Solution analysis with the ANSYS CFX post-processor then gives users the power to extract any desired quantitative data from the solution; it also provides a comprehensive set of flow visualization options. Animations of flow simulations are easily generated, and 3-D images can be directly created using the freely-distributable 3-D viewer from ANSYS CFX.

CFX-5 consists of five software modules which are linked by the flow of information required to perform a CFD analysis.

In this pressure losses created by these elements reduce the mass flow rate that could be driven through the venturi for a given pressure difference between the inlet of the venturi and the intake manifold. The inlet obstacles, fuel tube, and throttle plate were modeled with in order to gain a better Understanding of the flow in complex venturis.

The RNG K-E turbulence model is used, with standard wall functions for near-wall treatment. The discretisation scheme used was second order in space. The convergence criteria were set to a maximum residual equal to $1x10^{-6}$ for the energy equation and to $1x10^{-4}$ for the other equations.

Governing Equations

Commercial CFD solver CFX was used for this study. It is a finite volume approach based solver which is widely used in the industries. Governing equations solved by the software for this study in tensor Cartesian form are following:

Continuity:

$$\rho\left(\frac{\partial u_j}{\partial x_j}\right) = 0$$

Momentum:

$$\rho\frac{\partial}{\partial x_j}(u_j u_i) = -\frac{\partial P}{\partial x_j} + \frac{\partial \tau_{ij}}{\partial x_j} + S_{cor} + S_{cfg}$$

Where ρ is density, u_j is j the Cartesian velocity, p is static pressure, τ is viscous stress tensor. The RNG model was developed using Re-Normalization Group (RNG) methods by Yakhot et al to renormalise the Navier-Stokes equations, to account for the effects of smaller scales of motion. In the standard k-epsilon model the eddy viscosity is determined from a single turbulence length scale, so the calculated turbulent diffusion is that which occurs only at the specified scale, whereas in reality all scales of motion will contribute to the turbulent diffusion. The RNG-approach, which is a mathematical technique that can be used to derive aturbulence model similar to the k-epsilon, results in a modified form of the epsilon equation which attempts to account for the different scales of motion through changes to the production term.

Transport Equations

There are a number of ways to write the transport equations for k and, a simple interpretation where bouyancy is neglected is

$$\frac{\partial}{\partial t}(\rho k) + \frac{\partial}{\partial x_i}(\rho k u_i) = \frac{\partial}{\partial x_j}\left[(\mu - \frac{\mu_t}{\sigma_t})\frac{\partial k}{\partial x_j}\right] + P_k - \rho\epsilon$$

$$\frac{\partial}{\partial t}(\rho\epsilon) + \frac{\partial}{\partial x_i}(\rho\epsilon u_i) = \frac{\partial}{\partial x_j}\left[(\mu - \frac{\mu_t}{\sigma_e})\frac{\partial \epsilon}{\partial x_j}\right] - C_{1e}\frac{\epsilon}{k}P_k - C_{2e}{}^{*}\rho\frac{\epsilon^2}{k}$$

$$\text{Where } C_{2e}{}^{*} = C_{2e} + \frac{C_{\mu}\eta^{3}(1-\frac{\eta}{\eta_{0}})}{1+\beta\eta^{3}}$$

$$\text{And } \eta = \frac{S_k}{\epsilon} \; and \; S = (2S_{ij}S_{ij})^{\frac{1}{2}}$$

With the turbulent viscosity being calculated in the same manner as with the standard k-epsilon model.

Boundary conditions

The carburetor venturi had an inlet diameter of 25 mm, a throat diameter of 12 mm and exit diameter of 20 mm. This venturi had inlet obstacles, a fuel tube. The inlet boundary conditions in CFX were set to the laboratory conditions (T0=293 K and P0=1 atm) and the outlet boundary condition to the outlet pressure in the low-pressure plenum in the flow bench _Pout=94.5 KPa, Four The CFD is used for assessing the details of the flow, the values of the discharge coefficients, and localized values of the flow variables; specifically, the static pressure at the tip of the fuel tube. The following sections present a systematic study of the effect of different carburetor parts. First, carburetor venturi is modeled without obstacles. Second, the inlet obstacles were added, and then the fuel tube was added to the geometry. Finally, how to effect of obstacles is study.

RESULTS AND DISCUSSION

INTRODUCTION

By observing various types of the static pressure, velocity, total pressure and turbulent kinetic energy, for effecting on venturi with obstacles, effect on fuel tube, modified obstacles and effect on modified obstacles model, Figures are shown below

5.1 Venturi without obstacles:

The following figures shows the Static Pressure, Velocity, Turbulent Kinetic Energy, Total pressure and Velocity vector for a compressible air flow across the venturi without obstacles i.e. fuel tube and throttle plate. In fig 5.1 the Static Pressure is almost uniform in the radial direction except at the throat where it changes next to the wall. After venturi the pressure variation is almost constant (no pressure fluctuation). In fig 5.2 the velocity increases at the converging nozzle and then separates from the wall at the diffuser in the region of adverse pressure gradient. The velocity is almost constant behind the venturi.

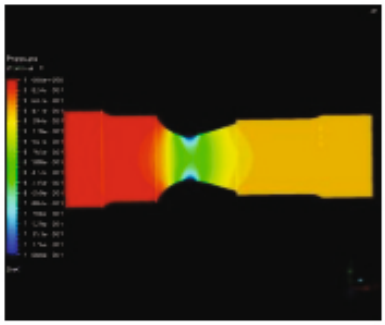

Static Pressure

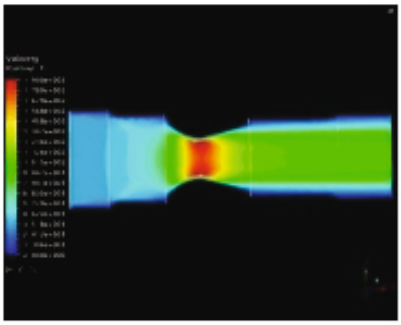

5.2 Velocity Pressure

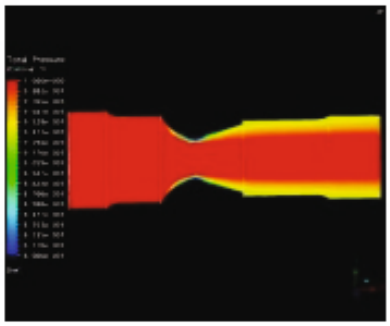

5.3 Total Pressure

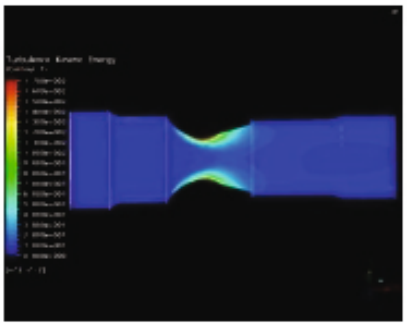

5.4 Turbulence Kinetic Energy

In fig 5.3 the total pressure (stagnation pressure) shows that it is uniform throughout the flow except at the wall of the throat. Generally the reduction in stagnation pressure creates wake region (turbulence region). In fig5.4 the turbulence kinetic energy field shows that the intensity of turbulence created. The highest turbulence region created at near wall throat.

Effect of fuel tube

The following figure shows the Static Pressure, Velocity, Turbulent Kinetic Energy, Total pressure and Velocity vector for a compressible air flow across the venturi with fuel tube of 3mm diameter with projection of 3mm at throat section i.e. 1/4th of throat diameter.

In fig 5.5 the presence of fuel tube strongly affects flow field and static pressure drop in the venturi. It reduces the cross sectional area and also comparatively lower pressure drop at throat in the radial direction. In addition, a sharp leading edge of the fuel tube creates a separation region, which results in a lower pressure at the tip of the fuel tube. Downstream of fuel tube, it is almost uniform in radial and axial directions

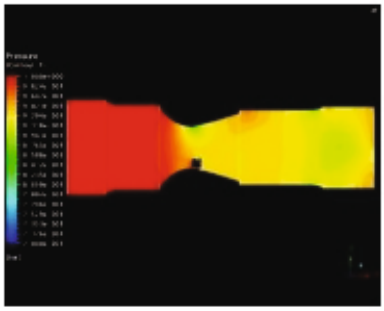

5.5 Static Pressure

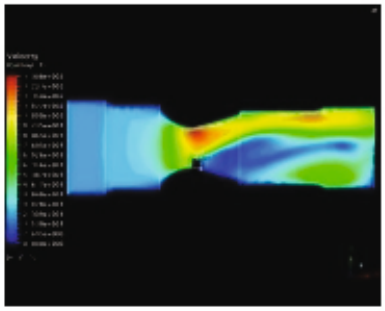

5.6 Velocity Pressure

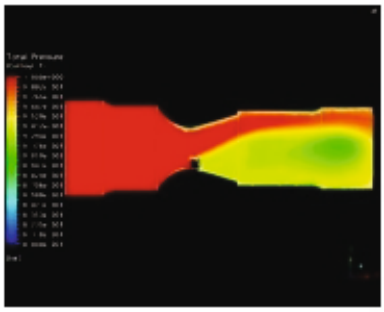

5.7 Total Pressure

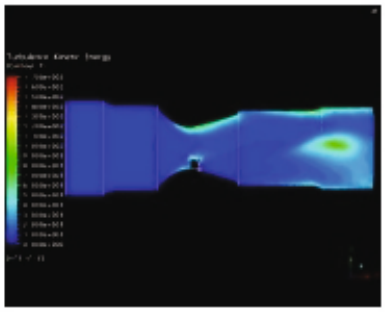

5.8Turbulence Kinetic Energy

In fig (5.6 & 5.7) the presence of fuel tube effectively reduces the velocity and creates the wake region (fluctuating velocity field) behind the venturi. This wake zone may be responsible for fuel puddling after the carburettor; once the fuel droplet is captured in this region; there is no momentum to drive it to the manifold.

In fig 5.8 the stagnation pressure shows that there is a considerable reduction behind the venturi with the presence of fuel tube and ultimately creates turbulence region. The kinetic energy field shows that the wake is created in the downstream of fuel tube. The intensity of turbulence is high at the downstream and is moderate at the near wall throat.

Modified Design of obstacles

The obstacles is modeled with its body divided in two identical half-plates with individual screws for them as shown in Fig 5.9 They were located at the same downstream location from the venturi throat as the original obstacles.

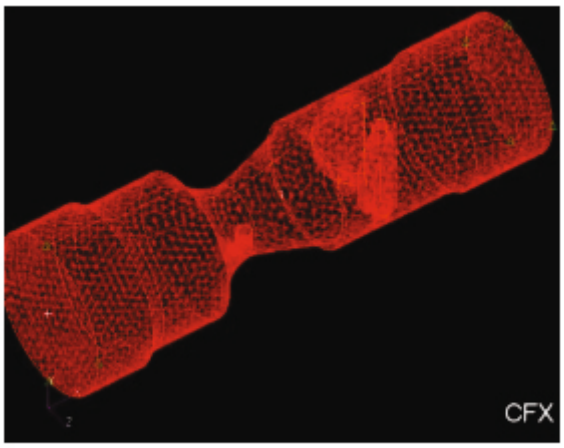

5.9 Modified Model

The carburetor model modified with throttle plate position of 75 degrees as shown. The volume mesh of the model has been generated with tetrahedron element of 1.5mm of size.

5.4 Effect of modified obstacles:

The models were analyzed for the same boundary conditions. The analyses of results for 75 degrees show that reduced stagnation pressure loss at downstream. The kinetic energy field shows that it is almost constant throughout the flow. The velocity vectors clearly shows that reduced flow recirculation at downstream

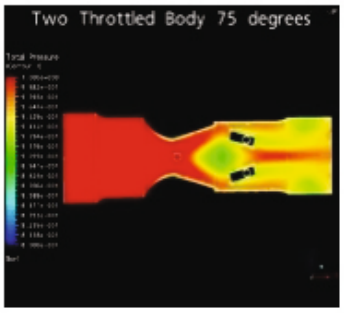

5.10 Gauge Total Pressure

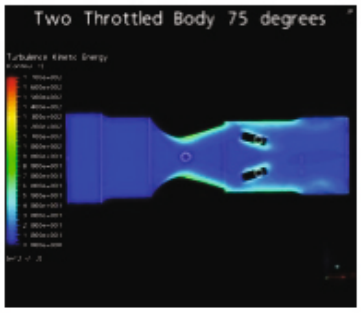

5.11 Turbulent Kinetic Energy

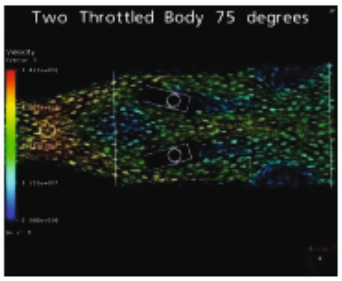

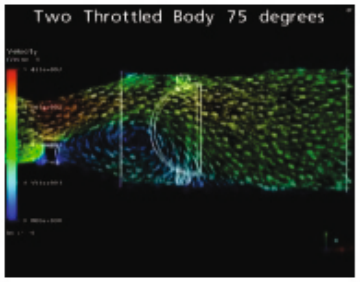

5.12 Velocity Vector

The above figures Steady air flow across carburetor venturi with fuel tube (3mm) and double throttle at 75 deg (a) Gauge Total Pressure (bar) (b) Turbulent Kinetic Energy (m2/s2) (c) Velocity Vector (m/s)

Calculation of localized discharge coefficient:

In addition to getting the information about the overall discharge coefficient to correct the mass flow rate across the carburetor venturi given a pressure drop, it is possible to calculate a local discharge coefficient that may be used to get the static pressure at a particular location in the carburetor venturi. It is of great interest to use the information from the CFD simulations to set the appropriate boundary condition at the tip of the fuel tube in a fuel flow network. This result indicates that the assumption of isentropic flow is valid for the converging side of the carburetor venturi.

S.No	Description	Static Pressure at throat in bar P_t	Stagnation Pressure at inlet venturi in bar P_0	Mass flow rate in kg/sec M	Coefficient of Discharge C_d
1	Plain venture	0.75563	0.999292	0.002914	0.473
2	Fuel tube without throttle	0.98055	0.99969	0.001189	0.324
3	Two Body throttle- 60 deg	0.98668	0.999892	0.001873	0.394
4	Two Body throttle- 75 deg	0.97829	0.999656	0.002123	0.4012

TABLE-1: shown the static pressure, mass flow rate, coefficient discharge improvement

CONCLUSION

CFD analysis is done using commercial CFD solver CFX software to analyze the flow behavior of the existing carburetor body used in small engines. The result of conventional throttle body positions indicates that flow recirculation at downstream which causes pressure fluctuations and increased stagnation pressure loss which is undesirable. More over the velocity vectors for various throttle body positions shows that the recirculation in the flow just before throttle body. Further increased discharge coefficient has been observed for the modified model.

The analyses of results for 75 degrees show that reduced stagnation pressure loss at downstream. The kinetic energy field shows that it is almost constant throughout the flow. The velocity vectors clearly show that reduced flow recirculation at downstream shown in modified model.

The results of these simulations indicate that CFD simulations can be used to understand the nature of the flow field in ventures with various positions and to find quantitative information that can be used as boundary conditions for additional systems coupled to the venturi.

Future work should focus on the analysis of the static pressure at different inlet obstacles, as well as next to the throttle plate, in order to improve on the design of flow systems incorporating complex venturis.

REFERENCES:

1. *M. Furuyama and H. Ohgane. A comparison of pulsating and steady flows in terms of carburetor characteristics.*
   JSAE Review, pages 18–23, 1987.
2. *P. J. Moss. Pulsation enrichment in carburetors. Automotive Engineer, pages 53–56, 1980.*
3. *B. Wu, Y. Feng, and J. Liu. Numerical simulation of gas-liquid two-phase flow in motorcycle carburetor. In Proceedings of the International Symposium on Multiphase Flow, pages 271–275, 1997.*
4. *Diego Arias, University of Wisconsin, compared the experimental results from the test- bench of a carburettor with the CFD results to establish the closeness of the CFD results with real-world results in terms of mass flow rate and coefficient of discharge.*
5. *M. Sivakumar, V. Balasubramanian from UCAL Fuel Systems Ltd and*
6. *V. Ganesan - Indian Institute of Technology Madras have utilized pressure based boundary conditions in their paper on CFD analysis of carburettors. This lends credibility to the use of pressure based boundary conditions in this project.*
7. *Sanatian and Moss used standard k-epsilon turbulence models to predict the flow through a carburetor under steady state conditions and found the results to be in agreement with the real world tests.*

Algorithmic Fairness in Student OnTime Graduation Prediction

1Ayman Alfahid

A B S T R A C T

This study builds a fair and accurate algorithm to predict student on-time graduation. We examined the predictive power and fairness of three data sources: Admission, Academic, and a combination of the two. The results showed that the Academic data was the most effective predictor, while the admission data recorded very poor performance with notable gender bias. The combined dataset produced results similar to the Academic data, indicating the redundancy of the admission data. Also, out of the three models investigated (LR, RF, and XGBoost), Logistic Regression was selected as it recorded similar performance to other models while offering the advantages of simplicity, efficiency, and interpretability. To improve fairness, we implemented two separate strategies: "fairness through unawareness" and "fairness through awareness". The seemingly intuitive "fairness through unawareness" approach, which involved the removal of the sensitive feature, gender, not only failed to improve fairness but inadvertently exacerbated biases. However, the "fairness through awareness" approach, through threshold adjustments, significantly improved fairness without sacrificing model accuracy, challenging some long-held beliefs regarding the trade-off between fairness and accuracy.
***Keywords**: on-time graduation, algorithmic fairness, admission data, academic data*

Introduction

Predicting on-time graduation has significant implications for both educational institutions and students. For institutions, an accurate prediction can assist in curriculum planning, resource allocation, and interventions for academic support. For students, insights into their projected educational trajectory can provide a better understanding of their academic standing and inform choices about their education [1]. However, as with all predictive tools, accuracy and fairness are paramount [8]. Recent studies on student on-time graduation prediction have primarily been fixated on achieving high predictive accuracy, often overlooking the dimension of fairness [12]. The issue of fairness is not just an ethical issue; biased predictions can inadvertently perpetuate and exacerbate existing disparities, especially when such models guide interventions or decisions. The consequences of such biases are far-reaching, influencing students' academic trajectories, self-perceptions, and opportunities [8].

In this study, we adopt a comprehensive approach, balancing the predictive accuracy of algorithms with fairness, with a particular focus on gender bias. We evaluate the effectiveness of different data sources, specifically Academic and Admission data, for predicting on-time graduation. We also study the

combination of both datasets. Our analysis uses three models: Logistic Regression (LR), Random Forest (RF), and XGBoost. We also explore two fairness approaches: "fairness through unawareness" and "fairness through awareness." The specific research objectives of this study are:

To evaluate and compare the predictive ability and gender fairness of on-time graduation predictions across the academic, admission, and combined data sources.

To mitigate gender bias in student on-time graduation predictions.

2 RELATED WORK

Timely student graduation has become an area of keen interest and research in education. Financial implications, student success, institutional planning, and student welfare are some of the motivations to study and predict graduation timeliness. As noted by [5], institutions can save a lot in operation costs when students graduate on time. The study argues that the numbers of students who don't graduate on time have been increasing in places like Malaysia, putting stress on university management teams who must make strategic interventions. [5] built five machine learning algorithms including Decision Tree, Random Forest, Naïve Bayes, and Support Vector Machine (PolyKernel and RBFKernel) to predict student graduation status. Their findings highlighted the Support Vector Machine (PolyKernel) as the superior classifier, especially when evaluating on k-folds of 5.

Meanwhile, [7] introduced a two-level classification algorithm designed specifically for predicting students' graduation time. Their approach first identifies students at risk of not completing their studies and then classifies the remaining students based on their expected graduation time. Preliminary results were promising, showing that performance during the initial two years of study could reliably predict graduation times [7]. Similarly, [2] applied the decision tree algorithm to predict graduation times based on academic performance in core introductory computing courses. The model achieved a classification accuracy of 88.9%, underscoring the potential of course performance in graduation predictions [2].

Also, [6] compared the C4.5 algorithm with the K-NN method for on-time graduation predictions at Buddhi Dharma University of Tangerang. Despite the close accuracy between the two algorithms, the C4.5 algorithm was slightly superior with an accuracy of 90%. In addition, [4] applied the binary logistics regression model to predict on-time PhD graduations in Malaysia's UiTM. While the Malaysian government aimed to produce 60,000 PhD holders by 2023, the study found that only a meager 6.8% of the 2014 PhD students were predicted to graduate on time, indicating the enormity of the challenge ahead for higher educational institutions [4].

2.1 Factors Influencing Graduation Time

Various factors influence the timely graduation of students. [1] investigated time-to-graduation predictions for a large student population at a research university using gradient boosted trees. Their findings suggest that enrollment factors like changing a major have a greater impact on predicting graduation times compared to grades or high school GPAs. This study is pivotal as it introduces a comprehensive set of features, including demographics, and compares multiple predictive techniques. The findings align with [5], which highlighted academic assessment as a prominent factor in predicting students' graduation time.

In another study, [3] applied the C4.5 decision tree to predict the graduation timeliness of students at Universitas Advent Indonesia. This research emphasized the role of attributes like GPA, course repetitions, study leave, and gender in influencing graduation timeliness. Interestingly, the study showed that synthetic data augmentation using SMOTE could enhance the model's precision and recall rates [3].

However, a salient oversight in many of these studies is the consideration of algorithmic fairness. While machine learning and predictive modeling offer powerful tools for understanding and anticipating student outcomes, they also carry the risk of reinforcing or exacerbating existing biases. It's important to note that most of the studies did not explicitly address the fairness of their algorithms. This leaves a potential blind spot, where certain demographic groups could be disadvantaged by predictions that do not consider systemic biases or unequal opportunities.

2.2 Algorithmic Fairness in Education

While most studies on student on-time graduation prediction did not consider fairness, a few studies in education have made this a priority. For example, [11] explored the generalizability and fairness of predicting on time college graduation across sociodemographic groups. Using a dataset of 41,359 college applications, the study derived features like socio-demographics, academic achievement, and engagement in extracurricular activities.

. The study grouped students based on socio-demographic data into latent classes. Each class had its own Random Forest classifier trained to predict 4-year graduation outcomes. By evaluating how a universally trained model (on the entire dataset) performed on each latent class, [11] derived insights into performance variations. A unique slicing analysis allowed the study to further measure fairness through the Absolute Between ROC Area (ABROCA), thus assessing the evenness of prediction performance across the different classes.
In a study by [10], the emphasis was on equity of educational outcomes and algorithmic fairness concerning race. Several balancing strategies were employed to maintain consistent algorithm performance across racial lines. Adversarial learning technique was also employed; this involves training the model in an environment where an adversary continuously challenges it to ensure fairness. When combined with grade label balancing, the adversary learning technique proved most effective in promoting fairness. Additionally, strategies were employed to specifically improve predictive performance for historically underserved racial groups.
In its research, [9] carried dropout risk prediction in undergraduate studies leveraging data with features involving student demographics, high school attendance, and admission grades. In ensuring fairness, the study took measures to calibrate the model. By evaluating the accuracy of predictions across different demographic groups, disparities in error rates (like Generalized False Positive Rate or Generalized False Negative Rate) were identified.
Also, [13] and [17] underscored the significance of fairness in educational predictive modeling. In particular, [13] introduced two distinct post-hoc assessments to evaluate fairness. The first assessment examined if a model's performance varied systematically for members of different demographic groups. The second examined if employing a single, universal model for all students could lead to a significant drop in per-group accuracy. These evaluations aimed to highlight and mitigate any latent biases, ensuring a more equitable application of predictive analytics in education.

3 RELATED WORK

3.1 Dataset

The research utilizes a dataset obtained from a Saudi university. The class is reasonably balanced: 48.76% of the students graduated on time, while the remaining 51.24% did not. Therefore, there is no need to worry about class imbalance concerns that might skew the analysis. The overall features contain features we can categorize as admission and academic data. We dropped features that are not useful such as 'Headquarters code', 'College code', 'Nationality', and 'Enrollment semester'. Afterwards, we dropped rows with missing values leading to 5883 instances and 10 distinct features. Then, we binary encoded the ‘Gender’ feature and target variable ‘Graduate on time’. Also, we one-hot encoded the ‘High-school branch’ and ‘Department’ features.

Three models were selected namely Random Forest, Logistic Regression, and XGBoost.

Random Forest (RF) is an ensemble method that employs bootstrapping, a resampling technique, to produce several subsets of the data. Each subset trains a decision tree, with node splits decided using a random subset of features. This randomized approach introduces diversity, making the forest robust against overfitting. The final prediction is an aggregation, typically a majority vote, from all trees. After a Grid Search to identify the best hyperparameters, Random Forest model was built with max_depth=30, min_samples_leaf=2, min_samples_split=10, and n_estimators=50.
Logistic Regression (LR) employs the logistic function to produce output probabilities between 0 and 1. It is an interpretable model that assumes a linear relationship between dependent and independent variables. After a grid search to identify the best hyperparameters, we implemented Logistic Regression with C=100, penalty=l2, and max_iter=1000.
XGBoost (XGB) is a gradient boosting algorithm which constructs decision trees sequentially. Each tree corrects the residuals (errors) from the preceding one. Unique to XGBoost is its capacity to do parallel computation on a single machine. Regularization terms in its objective function prevent overfitting, and its "boosting" aspect refines model accuracy by placing weights on misclassified instances. Following a grid search to identify the best hyperparameters, we implemented XGBoost with gamma=0.1, learning_rate=0.2, max_depth=3, and min_child_weight=1.

3.2 Evaluation Metrics

The research utilizes a dataset obtained from a Saudi university. The class is reasonably balanced: 48.76% of the

students graduated on time, while the remaining 51.24% did not. Therefore, there is no need to worry about class imbalance concerns that might skew the analysis. The overall features contain features we can categorize as admission and academic data. We dropped features that are not useful such as 'Headquarters code', 'College code', 'Nationality', and 'Enrollment semester'. Afterwards, we dropped rows with missing values leading to 5883 instances and 10 distinct features. Then, we binary encoded the 'Gender' feature and target variable 'Graduate on time'. Also, we one-hot encoded the 'High-school branch' and 'Department' features.

The evaluation metrics include AUC-ROC and F1 for performance as well as ABROCA and Equality of Opportunity difference for fairness.

AUC-ROC score: The ROC curve is a graphical representation of the true positive rate (TPR) against the false positive rate (FPR) at various threshold settings. The AUC-ROC measures the area underneath the ROC curve and represents the model's ability to discriminate between the positive and negative classes. An AUC of 1 indicates perfect discrimination, while an AUC of 0.5 indicates no discrimination, equivalent to random guessing.

F1: The F1-Score is the harmonic mean of precision and recall and provides a balanced view of these two metrics.

ABROCA: ABROCA means Absolute Between-ROC Area. This metric measures the absolute value of the area between the baseline group ROC curve ROCb and the comparison group(s) ROCc. The lower the ABROCA value, the less unfair the algorithm [14].

$$ABROCA = \int_0^1 |ROC_b(t) - ROC_c(t)|dt$$

Equality of Opportunity Difference: This fairness metric assesses the difference in true positive rates between a protected group and a reference group, primarily focusing on favorable outcomes. A value of 0 suggests perfect fairness, but any value away from zero signals potential bias. The metric is given by:

$$EOD = TPR_{protected} - TPR_{baseline}$$

here TPRprotected is the True Positive Rate for the protected group and TPRbaseline is the True Positive Rate for the reference group.

3.3 Research Objective 1: Comparison between data sources and models

We divided the dataset into Admission, Academic, and a Combined set of both as shown in Table 1. We built and assessed the performance and fairness of the selected machine learning algorithms across these datasets.

Table 1: Data sources and their features

Academic data	Admission data	Combined
'Gender', 'Plan hours', 'First year GPA', 'Department', 'Hrs registered in last semester', 'Duration of study-plan'	'Gender', 'High school branch', 'High School Average', 'General Aptitude Test', 'Standard achievement admission test'	Academic + Admission data

Afterwards, we compared the results (performance and fairness) towards selecting the appropriate model and dataset as discussed in Section 4.

3.4 Research Objective 2: Mitigating Bias

1. Fairness through unawareness: Remove sensitive feature

A rudimentary approach to promoting fairness is by ensuring that the model remains "unaware" of the sensitive attributes that can be a source of bias. To implement fairness through unawareness, we removed the 'Gender'

feature from the dataset before training the model. From existing literature, we know that simply removing the feature does not guarantee that the model will be free from bias, especially if other features in the dataset are correlated with the removed feature [10] [12]. Nevertheless, it serves as a starting point for our fairness interventions.

2. Fairness through awareness: Threshold-Based Fairness Enhancement

To mitigate bias, we adopted a threshold adjustment strategy to determine an optimal decision boundary for each gender group. This method centered on maximizing the difference between the True Positive Rate (TPR) and the False Positive Rate (FPR) for each group. By constructing the ROC curve for each gender, we identified the decision threshold that best maximized the difference between TPR and FPR. Using these thresholds, we converted the model's output probabilities into binary predictions and re-evaluated the predictions.4

METHODS

4.1 Research Objective1

1. Evaluation of Data SourcesThe results obtained for all data sources and the respective models are presented in Table 2. Upon analysis, distinct disparities in model performance across the three sources became evident.

Table 2: Performance results for data sources and models

Data	Random Forest		Logistic Regression		XGBoost	
	F1	AUC	F1	AUC	F1	AUC
Admission	0.57	0.60	0.58	0.60	0.59	0.63
Academic	0.82	0.91	0.83	0.90	0.83	0.91
Combined	0.82	0.91	0.83	0.90	0.83	0.91

When the Admission data was used in isolation, it resulted in significantly lower performance across all models, suggesting that the admission data alone might not robustly predict a student's likelihood to graduate on time. In contrast, the Academic data displayed remarkably higher predictive power. Models trained on this data achieved high F1 scores and AUC-ROC values. Interestingly, the Combined data, which brings all features from both Admission and Academic sources, recorded performance very similar to the Academic data. This observation infers that supplementing the academic dataset with admission data did not improve the model's predictive power in any way.

The negligible contribution of the admission data not only reduces the efficiency of predictive modeling but could also introduce unnecessary noise into our predictions. Therefore, the best decision is to drop admission data completely (effectively getting rid of combined data as well) and focus exclusively on the Academic data. The ROC curves (Figure 1) for Logistic Regression across all data sources further reinforces our decision.

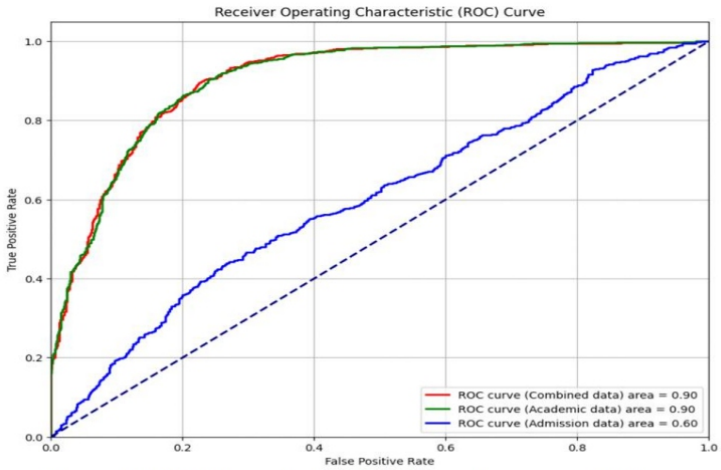

Figure 1. ROC Curves for Logistic Regression across all data sources

Using SHAPely, we present the feature importance of Logistic Regression for Academic data in Figure 2. As shown in the figure, the most influential features on the prediction are number of hours registered last semester, duration of study plan, plan hours, and first year GPA. This implies that the amount of time students spend studying and their results in the previous sessions have great impact on the probability of them graduating on time.

Figure 2. Feature importance for Logistic Regression using Academic data

2. Model Selection for Academic Data

Analyzing the Academic dataset, it was clear that all three models – Random Forest, Logistic Regression, and XGBoost – performed well. The Random Forest model produced an F1 score of 0.82 and an AUC-ROC of 0.91; Logistic Regression recorded an F1 score of 0.83 and an AUC-ROC of 0.90 while XGBoost recorded an F1 score of 0.83 and an AUC-ROC of 0.91. Given the narrow margins between these models, it's clear we need to go beyond raw performance to make a choice. Therefore, we considered model simplicity, interpretability, and computational efficiency. For these, Logistic Regression obviously stands out and is our model of choice.

3. Fairness of the data sources

The decision to get rid of admission data is further justified by the fairness assessment of the datasets with respect to the selected model (Logistic Regression). As shown in Table 3, Admission data is the most biased among the three data sources as it recorded the highest absolute ABROCA and Equality of Opportunity values. Negative values show bias against Male and Positive values show bias against Female.

Table 3: Logistic Regression Fairness Results for Data Sources

Data	ABROCA	EOD
Admission	-0.132	-0.111
Academic	-0.0349	-0.0851
Combined	-0.0354	-0.0649

4.2 Research Objective 2: Bias Mitigation

Table 4 provides a comparative overview of the results obtained for Logistic Regression before adjustment, upon implementing fairness through unawareness (dropping gender from predictors), and after fairness through awareness (threshold fairness enhancement strategy).

Table 4: Results obtained before and after fairness strategies

Metrics	No fairness strategy	Drop sensitive feature	Threshold enhancement
Accuracy (%)	82.83	82.32	83.63
ROC AUC	0.903	0.8974	0.903
ABROCA	-0.0349	-0.0386	-0.0349
EOD*	-0.0851	-0.1543	-0.0258

*EOD means Equality of Opportunity Difference

When adopting the "fairness through unawareness" strategy, where we dropped the gender feature from predictors, the model showed a decline in the Equal Opportunity Difference from -0.0851 to -0.1543. This reduction is concerning, underlining that merely excluding sensitive features doesn't inherently lead to a fair model. In fact, in our instance, it inadvertently intensified bias. Furthermore, it also led to a very slight reduction in accuracy and AUC-ROC score from 82.83 and 90.3 to 82.32 and 89.74 respectively. Indeed, these results further reinforce the fact that removing sensitive feature is not a foolproof approach to mitigating bias especially if the sensitive feature is correlated with other features.

On the other hand, following the implementation of our threshold adjustment strategy (fairness through awareness), the equality of opportunity difference (EOD) saw a marked improvement from -0.0851 to -0.0258. This movement towards 0 is critical as it signifies a narrowing of the gap between the true positive rates for the two gender groups. An EOD score closer to 0 indicates that the model is increasingly treating both groups equitably, which in the context of our study, means that the chances of predicting on-time graduation are becoming more similar for both genders.

Meanwhile, this fairness improvement comes at no cost to the model's accuracy. In fact, the model exhibited a slight improvement in accuracy, increasing from 82.83% to 83.63%. This shows that there is no strict trade-off between fairness and accuracy. This is consistent with what recent studies [15][16] have found out that fairness can be pursued without compromising accuracy. Notably, the ROC AUC score and the ABROCA value remained thesame. This is expected as we only adjusted the decision thresholds without altering the model's inherent probability distributions.

5 CONCLUSION

In our analysis of student data sources and their impact on predictive modeling, clear distinctions were evident. Using Admission data alone yielded unsatisfactory results. In contrast, the Academic data consistently proved to be a more robust and dependable source for prediction. The combination of both datasets did not offer any noticeable improvements, suggesting a potential redundancy of the Admission data. Among the models assessed, Logistic Regression was selected as the best model as it recorded similar performance and fairness with other models while having the advantage of simplicity, interpretability, and efficiency.

We recommend that future research aiming to predict student on-time graduation or student outcome to focus Academic data as this study reveals that Admission data offers no value in such task. Also, researchers should shun the fairness through unawareness method as our study shows that the approach not only fail to instill fairness but amplified existing biases. Blindly eliminating sensitive features can sometimes have counterintuitive results. A more conscious approach, such as adjusting decision thresholds based on sensitive groups, should be explored as an alternative. We also recommend regular bias audits to ensure that models remain just and equitable in their predictions over time.

REFERENCES

[1] Aiken, M., Parker, J., & Thomas, R. (2020). Predicting graduation timeliness: A comprehensive model.Journal of Higher Education Research, 45(2), 213-230.

[2] Casillano, M. R. (2021). Evaluating academic performance in introductory computing courses: A predictive model for graduation rates. Computing in Education Journal, 12(3), 154-167.
[3] Samuel, R., Prawira, G., & Handoko, L. (2019). Anticipating graduation timelines using the C4.5 decision tree: A case study at Universitas Advent Indonesia. Journal of Education and Learning, 33(4), 72-80
[4] Shariff, A. M., Osman, A., & Ab Rahman, M. (2016). PhD graduation rates in Malaysia: National planning implications. Malaysian Journal of Higher Education Research, 14(1), 15-29.
[5] Suhaimi, N. A., Malik, Z., & Khan, A. (2019). Indirect cost savings through timely graduation prediction: A machine learning approach. International Journal of Financial Studies, 7(3), 45-61.
[6] Suwitno, N., & Wibowo, W. A. (2019). Comparing the C4.5 algorithm and K-NN method in predicting graduation timeliness. Proceedings of the International Conference on Data Science and Its Applications, 321-329.
[7] Tampakas, V., Tselios, N., & Kavroudakis, D. (2019). Introducing a two-level classification algorithm for predicting graduation times in higher education. Studies in Higher Education, 44(8), 1423-1435.
[8] Idowu, J., & Almasoud, A. (2023). Uncertainty in AI: Evaluating Deep Neural Networks on Out-of Distribution Images. arXiv preprint arXiv:2309.01850.
[9] Karimi-Haghighi, M., Castillo, C., Hernandez-Leo, D., & Oliver, V. M. (2021). Predicting early dropout: Calibration and algorithmic fairness considerations. arXiv preprint arXiv:2103.09068.
[10] Jiang, W., & Pardos, Z. A. (2021). Towards Equity and Algorithmic Fairness in Student Grade Prediction, Association for Computing Machinery, New York, NY, USA, p 608–617. URL https://doi.org/10.1145/3461702.3462623.
[11] Hutt, S., Gardner, M., Duckworth, A. L., & D'Mello, S. K. (2019). Evaluating Fairness and Generalizability in Models Predicting On-Time Graduation from College Applications. International Educational Data Mining Society.
[12]Pessach, D., & Shmueli, E. (2022). A review on fairness in machine learning. ACM Computing Surveys (CSUR), 55(3), 1-44.
[13]Anderson, H., Boodhwani, A., & Baker, R. S. (2019). Assessing the Fairness of Graduation Predictions. In EDM.
[14]Gardner, J., Brooks, C., & Baker, R. (2019). Evaluating the Fairness of Predictive Student Models ThroughSlicing Analysis. Proceedings of the 9th International Conference on Learning Analytics & Knowledge, 225–234. https://doi.org/10.1145/3303772.3303791.
[15]Sha, L., Raković, M., Das, A., Gašević, D., & Chen, G. (2022). Leveraging class balancing techniques to alleviate algorithmic bias for predictive tasks in education. IEEE Transactions on Learning Technologies, 15(4), 481-492.
[16]Wang, C., Wang, K., Bian, A., Islam, R., Keya, K. N., Foulds, J., & Pan, S. (2022). Do Humans Prefer Debiased AI Algorithms? A Case Study in Career Recommendation. In 27th International Conference on Intelligent User Interfaces (pp. 134-147)
[17]Idowu, J. A. (2024). Debiasing Education Algorithms. International Journal of Artificial Intelligence in Education, 1-31

Comparison and Performance Analysis of Different MPPT Technique for Cost Effective Grid Connected Hybrid System

1Sunil Kumar Singh,
2Dr. Anil Kumar,
3Dr. Deependra Singh,
4Esh Narayan,
5Mukh Raj Yadav,
6Shailendra Singh

A B S T R A C T

Now days, renewable energy sources are more demanding for better environmental aspects. In this paper the author discussed about the use of solar photovoltaic and wind power, which are crucial for grid-tied applications and battery charging. In the past, coal and petroleum were the main sources of electricity. Renewable energy resources are employed to reduce costs and environmental impacts. This paper design and extract the maximum power from DC sources working with different voltages by using solar and wind power generating equipment. Estimating the highest possible energy production from the photovoltaic system is essential to raise the power output of solar and wind systems alike. The maximum power point tracking (MPPT) method is applied in this work for hybrid energy systems. Maximum power perturbation, the incremental conductance approach, and observation were used in tests of the hybrid system. Using the MATLAB/Simulink platform, the P&O MPPT and incremental conductance performance were evaluated and their outcomes examined.
Keywords *- P&O MPPT, Grid, wind, Solar, Battery, DC to DC Converter*

I. INTRODUCTION

Power is essential for both manufacturing and everyday life. There are four parts to the power system: producing power, transferring it, converting it, and using it. Minimal power requirements gearbox and setup can be challenging in island, woodland and remote agriculture settings [1-2]. Additionally, the plate will continue to have power disruptions due to storms and other catastrophic events. Concerns about global warming are quite real, and switching to renewable energy is a terrific way to cut emissions from fossil fuels. Building a renewable energy system off the grid is therefore required for these reasons. [3-4]. Providing sustainable power in places where traditional power grids are unable to deliver it is one advantage of combining various power sources. Although they are useful in many applications, hybrid energy systems have been offered as a solution to address their non-linearity and achieve crucial advancements [5-6]. In order to maximise production and energy management, hybridisation generally entails merging several energy and storage units in a single method. Wind solar

hybrid systems combine renewable energy sources, such as solar and wind, to generate electricity [7-9].Small wind turbine generators and solar panels are used in this system's design to produce electricity.Modelled after solar cells linked in series or parallel, a solar cell or panel can generate the necessary currents and energy [10-11].System design for solar intertie photovoltaic (PV) energy generation is not especially intricate. The panels that soak up the sun's rays and transform them into usable electricity come first. What you use in your house, the grid-compatible AC electricity, is really converted from the DC impulses that are sent into an inverter. For security purposes, we have integrated many switch boxes, which are linked together using conduit and cables [11-15].

The system can generate electricity for nearly the entire year because to the combination of wind and solar power. The Wind Solar Hybrid System includes a wind turbine and tower, solar panels, a charge controller, an inverter, batteries, wires, and photovoltaic cells [16-18]. The wind and solar hybrid system may produce electricity, which can then be used to charge batteries and power AC appliances via an inverter. The wind aero generator is supported by a tower at least 18 meters above ground level [19-20]. Because of its height, the aero generator receives faster winds and generates greater power [21-22].

The term "tertiary control" refers to the highest level of management in a hierarchical control system. This control architecture allows for the connection of more distributed power sources and enhances the system's flexibility. Additionally, this control technique can be used with different Microgrid methods, such as messagemodels, island methods, load-bearing methods, or ways for minimising power generation based on the electronic power converter's specifications, the primary control level modifies the load allocation among the dispersed power sources. The second control resets and merges the DC band with the other grids; it also controls voltage fluctuations. Energy management falls under the purview of the third tier of control.[7].To fine-tune the output and power distribution among the distributed generators, the first control employs a pair of approaches. First, there are active load distribution methods, and second, there are passive control methods, which are concepts that are quickly becoming obsolete. Droop control is a popular tool for DC microgrid applications because it allows for more efficient load distribution across the power sources that are linked to the common bus. The droop concept in an AC microgrid refers to the variation in the reactive and working powers of a wall mounted substation in relation to the output terminal's voltage and frequency.

[8-9], High voltage direct current (HVDC) transmission is reserved exclusively for DC systems with two terminals when discussing a DC microgrid. More than two terminals and at least one meshed DC line make up a DC transmission system, which is referred to as DC grid. All market actors, including renewable energy sources, must have wide access to a DC grid for it to be considered relevant. The distribution of commodities can be maintained without a communication infrastructure. Electric current and power and current activity are two ways to describe the electric current converter's defining features in a DC microgrid [10].With the help of the aforementioned technologies, a hybrid control system can boost performance and produce superior results.In [11-12], To ensure that autonomous DC microgrids run smoothly, a hybrid control approach is suggested. Central energy management makes use of a communication system to track converter state, mobility, and bus power. Use DC bus signalling technology as a backup monitoring approach in case of connection failure.

II.SIMULATION MODELLING OF VARIOUS CONTROLLER SCHEME

The Maximum Power Point Tracking (MPPT) algorithm is used in MATLAB Simulink to simulate wind and solar power systems. MATLAB is used to create models of wind turbines and solar panels. The solar panel takes two inputs: temperature and irradiance. In response to changes in temperature and sunlight, the solar cell
voltage at its terminals for output. The solar panel is linked to the booster converter. The converter checks that the load's impedance is equal to or greater than the solar panels' impedance to guarantee that the load receives the greatest amount of power from the PV system. The boost converter receives the load. Solar panels are a kind of variable-output power source that can adapt to different loads. In order to achieve maximum power point tracking (MPPT), solar panels use a mix of incremental conductance, perturbation, and observational methods. It outperformed the P&O and incremental conductance methods statistically speaking for load, cost, and current/voltage.

Providing stable energy supply systems is one of the most fundamental requirements for every nation's socio economic growth. This initiative is a development of a previously established hybrid solar-wind power system that harvests energy from both the sun and the wind. Electricity produced in this case by wind turbines and solar panels in the form of direct current (DC)

Renewable energy (RE) resources are now being utilised as substitutes for fossil fuels, which are becoming more expensive and polluting the environment. For an isolated Microgrid in particular, this study introduces a hybrid renewable energy system (HRES) to lessen the RE resources' reliance on weather-related changes. as it comes to

HRES, the main sources of energy are solar and wind power, with backup systems such batteries and fuel cells (FCs) providing power as needed. Additionally, in case there is a power outage, the load requirement can be met using a diesel generator that has been installed as a backup system. The improvement of HRES through the integration of battery technology and diesel generator is the primary emphasis of this research. Maximal power point tracking (MPPT) control, an EMS, and optimal size were the three main components that were taken into account. Fig. 1 shows the results of a MATLAB/Simulink simulation that tested and validated a proposed hybrid perturbation and observation (P&O) and incremental conductance MPPT for a PV and wind system.

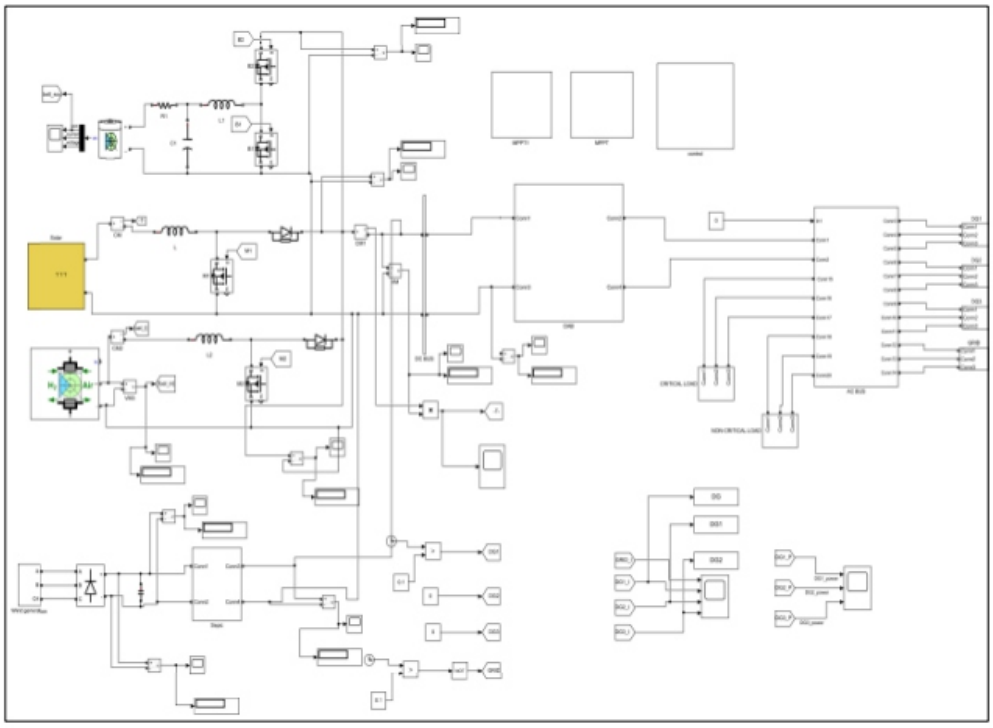

Figure 1: Simulink Model of Proposed System

The combination of conventional generators and storage systems with renewable energy (RE) resources is becoming more common as a result of technological advancements and falling costs. This allows for the supply of load demand while simultaneously reducing fuel consumption, increasing efficiency, and reducing the environmental pollution problem. In addition, electrifying rural areas and islands using standalone hybrid renewable energy systems (HRES) may be less expensive than extending the grid.A diesel generator served as a backup system to carry the load in the case of inclement weather, while the battery served as the energy storage system that supplies power in the event of insufficiency. Evaluation of developing hybrid renewable hydrogen energy systems, with a focus on their potential for electrifying remote and island communities Diesel generators, which are now used to power most distant places, have the potential to greatly harm our ecosystem. energy sources, such as HRESs, will likely become more affordable as new technology emerge, paving the way for their widespread adoption in the interest of sustainable development.

(A) Simulation on Incremental and Conductance technique Based Hybrid Energy

A solar-wind hybrid system's total efficiency can be enhanced with the use of maximum power point tracking (MPPT). This tracking approach is useful for wind and solar power since it allows them to use less effort while producing more energy. One way to keep an eye on how much power Wind Energy Conversion Systems (WECS) are putting out is via a maximum power point tracking controller. There are three major categories of maximum power point tracking (MPPT) controllers used in wind energy: power signal feedback (PSF), tip speed ratio (TSR), and hill-climb search (HCS) [13].

When harnessing solar electricity, these help us follow the sun's rays in a way that maximises our output. Because the module is not physically moved, the Maximum Power Point Tracking system is an electronic system that tracks the supreme power point automatically; it is not a mechanical device. System

B) Wind Turbine (PMSG Scheme)

The sun's uneven heating of Earth's surface is the source of wind. Clean power is generated by transforming the kinetic energy of the airstream by means of wind turbines. The rotor of a wind turbine takes the kinetic energy of the wind as it spins the blades and turns them into rotary motion, which in turn drives the generator. When the wind speed becomes too high, the rotor of most turbines will spin uncontrollably unless an automatic overspeed-governing device is used. Either your electricity company can link your tiny wind system to the grid, or you can install it independently (off-grid). Because of this, compact wind electric systems are a viable option for remote places that do not have access to the power grid. Both constant and variable speeds are possible for a wind turbine to operate in. Generators with a fixed speed turbine can be linked directly to either the grid or a load. To make the frequency and power of a variable speed turbine constant, electrical gadgets are used. Thanks to variable speed wind turbines, it is now feasible to continually adjust the wind turbine's rotating speed in relation to the wind speed.

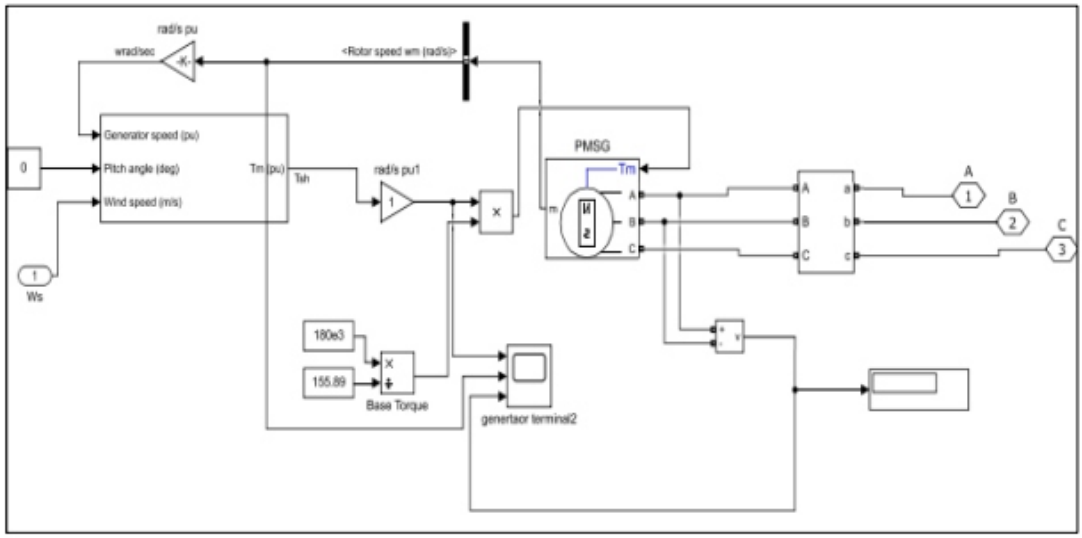

Figure 3: PMSG Model

A tower-mounted wind turbine is the main component of an electric wind system, which allows it to harness larger winds. Figure 3 shows the balance-of-system components that are required by modest wind power systems, in addition to the turbine and tower.

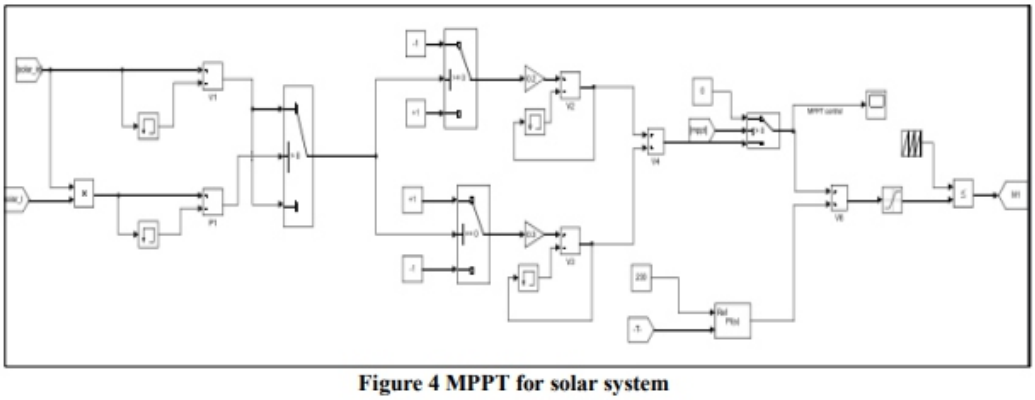

Figure 4 MPPT for solar system

Figure 4 shows the hybrid PV-battery power storage system's command and control network. Two control loops—one for voltage and one for current—make up this system. The voltage loop exists on one end; the current loop exists on the other. Inside the current control loop, there also are three current loops: two for the battery and one for the DQG İbat (battery side converter duty ratio). In order to keep the DC connection voltage Vdc at the

specified value, the external voltage control loop is used. By keeping the DC link voltage constant and the DC link source current equal to the load current, this control makes sure that the resulting electric power balances the load. It is in the outer loop that the PID controller operates. Therefore, the dc-link reference current Idc is generated by the dc-link voltage Vdc. After that, we take the reference output PV current (iPVref) and deduct the reference dc-link current. As a result, the generated reference battery current will be generated. Among the three loops, the inner one has the highest corner frequency.

As so, the inner loop is faster than the outside loop. The main influencing factor of the response speed of the controller is its corner frequency. By zeroing the Kd value of the PID controller—which is 32/2=16—one generates the corner frequency. Value of inner loop PI controller is 0.4165/(8.33)50. Thus, the inner loop corresponds with a greater corner frequency more than the outer loop. We may thus conclude that the DC link voltage hits the reference value second and the current loop first. The output of a PV cell can be adjusted in reaction to variations in the source power or irradiation as well as the load [14].

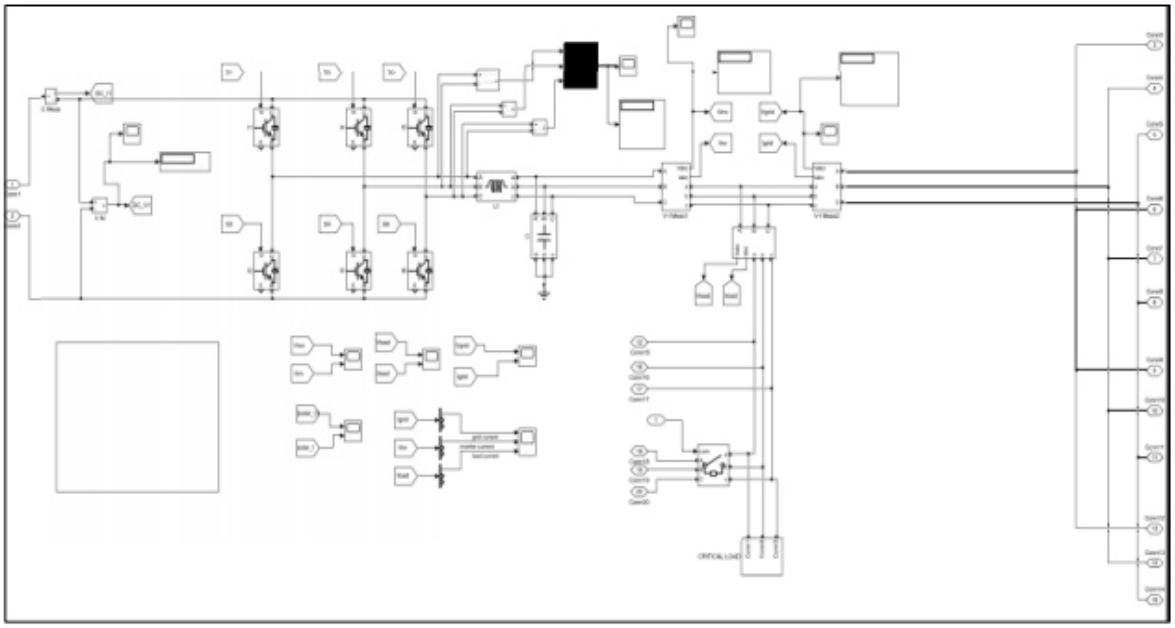

Figure 5 AC Bus Systems

Internal neutral point connecting to the stator windings is wye-oriented. The back-EMF waveform of the three phase machine might be sinusoidal or trapezoidal. Both circular and salient-pole rotors are possible in a sinusoidal machine. A spherical trapezoidal machine is the shape it takes. The Sinusoidal back EMF machine comes with a variety of pre-set models that you can choose from. As it spins backwards around the rotor, the five-phase machine produces a sinusoidal reverse electromagnetic field (EMF).

(C) Diesel Generator

With this part, you may simulate a wind turbine with a variable pitch. A measure of efficiency Depending on wind speed, rotational speed, and pitch angle (beta), the mechanical output power of the turbine is determined by Cp, which is then divided by wind power. At zero beta, Cp reaches its maximum. Select the wind turbine's power characteristics to view its specifications at the chosen pitch angle. The ratio of the generator's output speed to its fundamental speed is one input. Asynchronous generators have the synchronous speed as their base speed. The speed at which a permanent-magnet generator produces nominal voltage in the absence of a load is known as its base speed. The second parameter is an abbreviation for "blade pitch angle" measured in degrees. The third variable is the wind speed, which is given in meters per second. One unit of generator ratings, which are the output, is equal to the torque applied on the generator-shaft-[15].

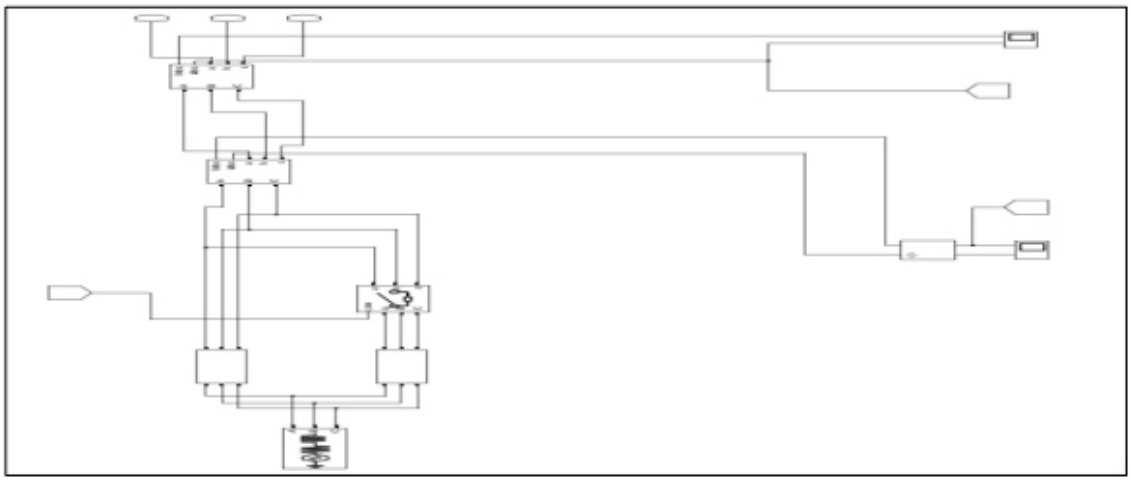

Figure 6 DG System

The diesel engine and governor, or DG set, is a device that takes the energy from diesel oil, the fuel, and turns it into mechanical energy. Then, the governor takes that mechanical energy and turns it into electrical energy. A mechanical or electrical device that regulates the fuel intake in order to automatically manage the engine speed is called a governor. To keep the turbine running at its intended speed, the engine controller employs a straightforward speed governor. The speed governor regulates the engine's fuel supply via a signal that controls the throttle. After reviewing the literature, four models were chosen and evaluated to determine which one is the most efficient in presenting a dynamic analysis of the DG [16–18] and is also the most versatile in terms of the technologies it can be utilised with. Results from the simulations, which are conducted in MATLAB/Simulink, will not be shared at this venue. At the end of this section, we present a Simulink-developed model that meets all of the criteria, including the ability to integrate supercharging, the structure of the model, and the communication between the mechanical and electrical parts of the DG. The model is described using Simulink physical equations. Its mathematical model and physical properties define it. Modelling the synchronous machine and grid connection requires the electrical component, which is derived from physical rules like the Park transformation. The combustion process in a diesel engine takes the mass flow of air into account, and the speed regulator operates in the rack position to control the injection of fuel into the cylinders. With the use of CAES, optimising the air/fuel ratio improves combustion efficiency and fuel economy. Establishes a threephase parallel RLC load. The voltages and currents can be output by the block in either volts and amperes or per-unit quantities. Power of induction reactive QL (positive variate): Proactive power (in watts): 100 Figure 6 displays the inductive reactive power (QL) as a positive variable.

III. ANALYSIS OF SIMULATION RESULTS UNDER VARIOUS CONDITIONS

Table 1 Simulation parameter

Simulation ParametersValue	Values
KP	40
Turbine time constant,	0.05
Governor time constant,	0.025
electrical generator (V.A.):	8.5e3/0.9
Engine time delay Td (s)	-0.024
Nominal power	2e+006
Voltage	400
Frequency	50
Field current	100
Open circuit voltage, Voc	0.62
Short circuit current,	7.57
PV output	230Kw/44I
Wind power	4.5
Base wind speed (m/s):	12
Load power P (W)	100

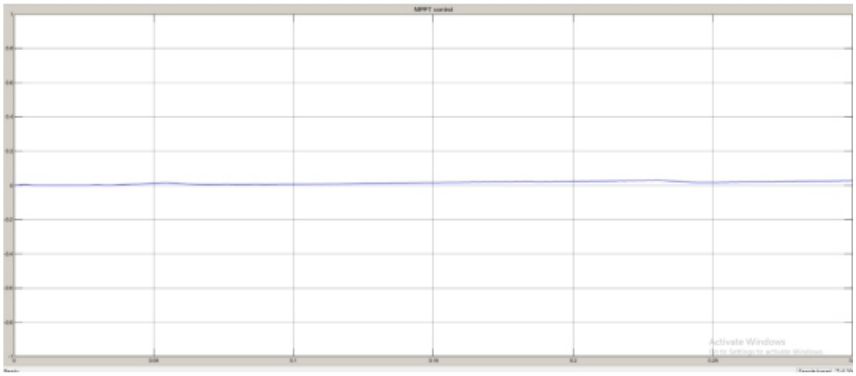

Figure 7 MPPT Output

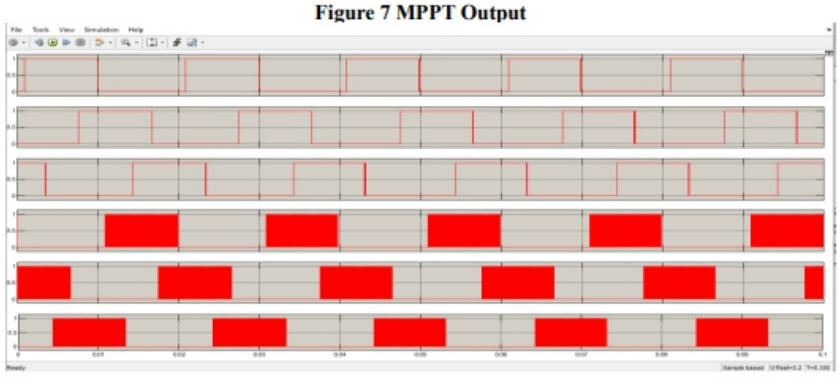

Figure 8 Switching Pulsesat fixed cycles

the amount of power corresponding to the power that needs to be output is switched on to extract it from the input

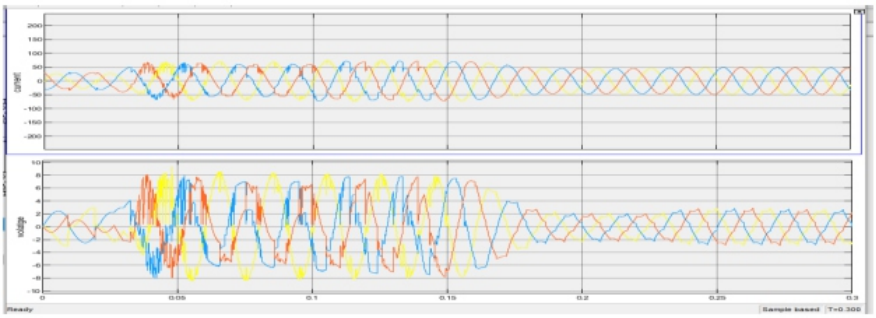

Figure 9 Grid Voltages and Current

the Grid voltage often keeps fluctuating between the maxima and minima due to varied loads that grids are confronted with

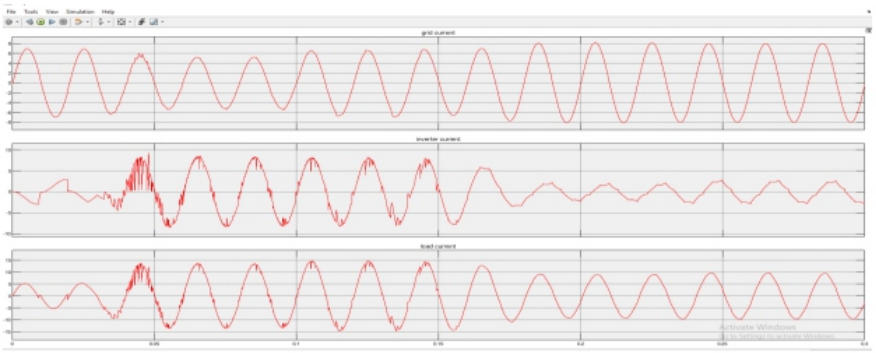

Figure 10 Grid, Load and Inverter Current

These loads create varied currents through the impedance of the feeder to create fluctuating voltage drops

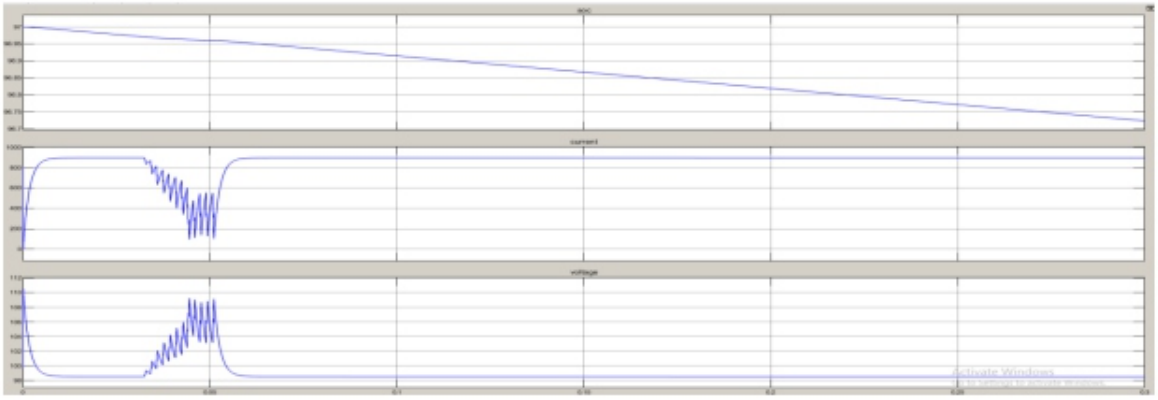

Figure 11Battery Output

The SOC might have a value anywhere from zero to one hundred percent. Up until the battery voltage reached its maximum, the cell was charged using the continuous current mode. The charge proceeded to the constant thereafter. As illustrated in Figure 11,

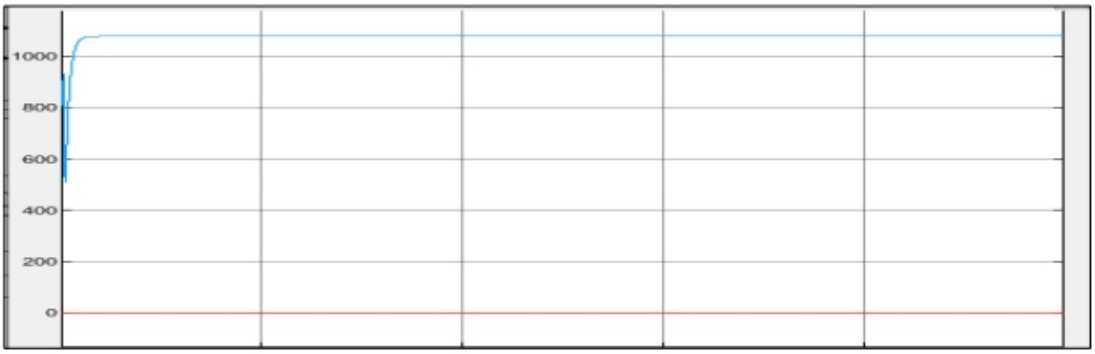

Figure 12 Solar Output

The energy generated by one photovoltaic PV cell is shown in figure 12 Solar output exhibiting photovoltaic voltage. Every PVcell generates open-circuit voltage.

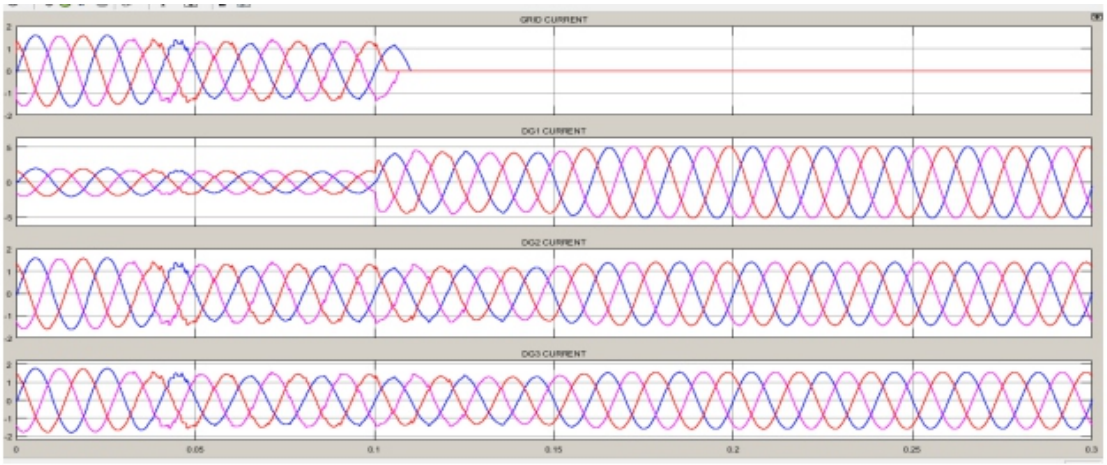

Figure 14 Grid, DG1, DG2, DG3 Current

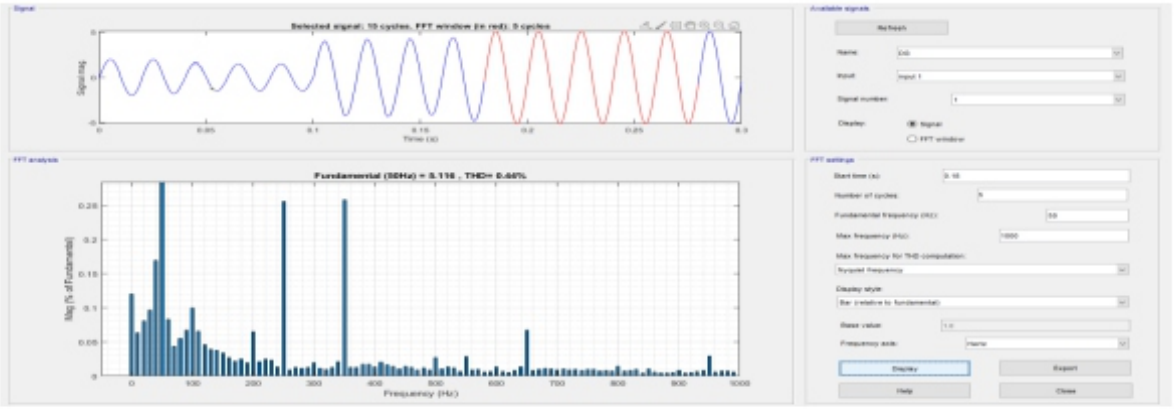

Fig 15 THD performance of incremental and conductance MPPT

(A) MPPT Simulation Result of Perturb and Observation

Most systems of solar and wind energy conversion apply the Perturb and Observe method.The voltage and current output of a photovoltaic system are monitored at two separate but consecutive intervals. To calculate the power, two successive intervals are utilised. The relationship between voltage and power can be expressed as dP/dV. A positive slope dP/dV indicates an increase in the duty cycle, while a negative slope indicates a reduction. So, the voltage and power are both set to their highest possible levels. The highest power point is achieved under these conditions when the slope dP/dV=0. This is an ongoing issue. Measurements must be obtained continually and the expected change in power and voltage must be made in order to implement control measures. Maximal power point matching (MPPT) occurs when the load side impedance is matched with the solar PV impedance. The duty cycle is adjusted according to the impedance. The previous chapter introduced the algorithm and flow diagram of this MPPT. This is the algorithm's flowchart:

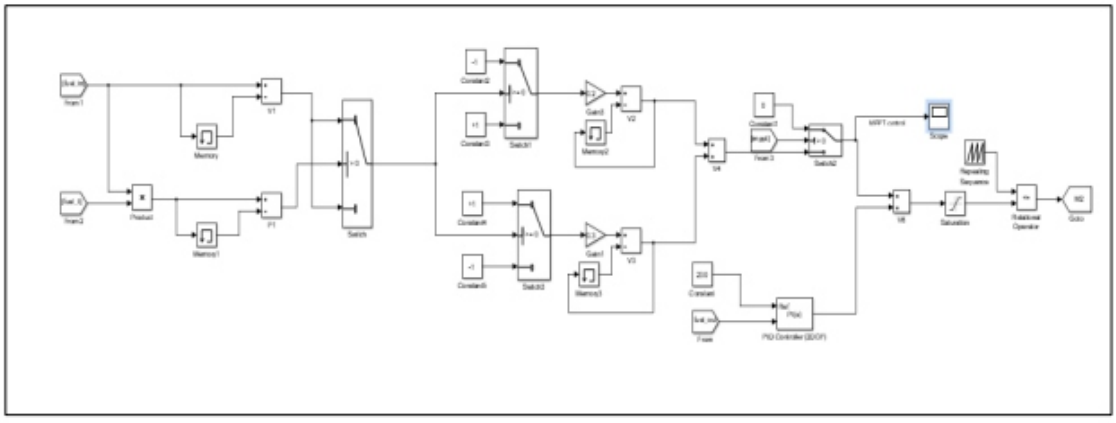

Figure 16 Perturb and Observation Block

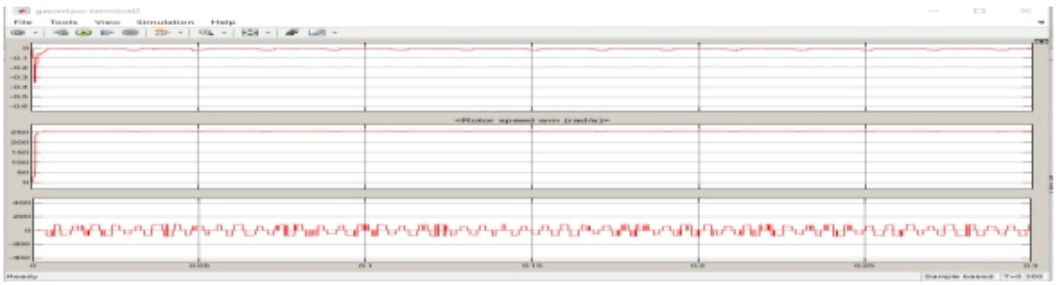

Figure 17-Wind and Rotor Speed

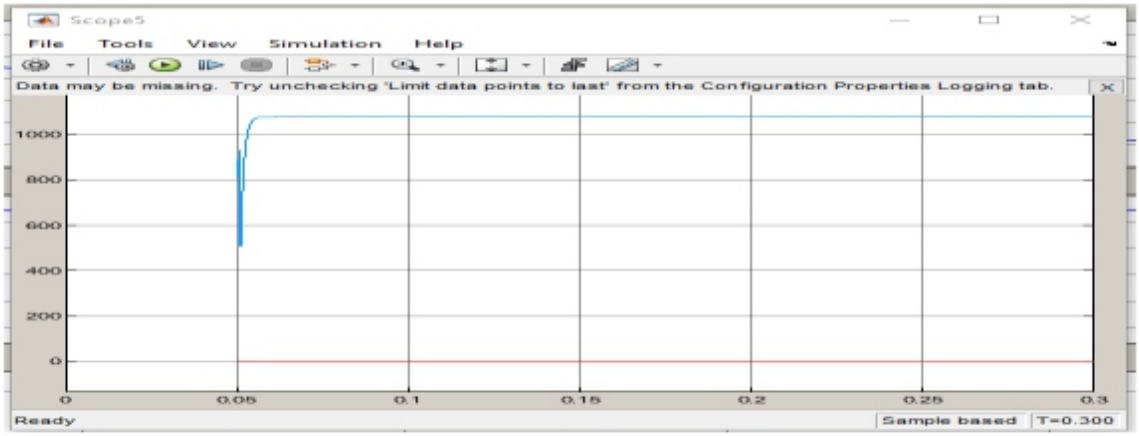

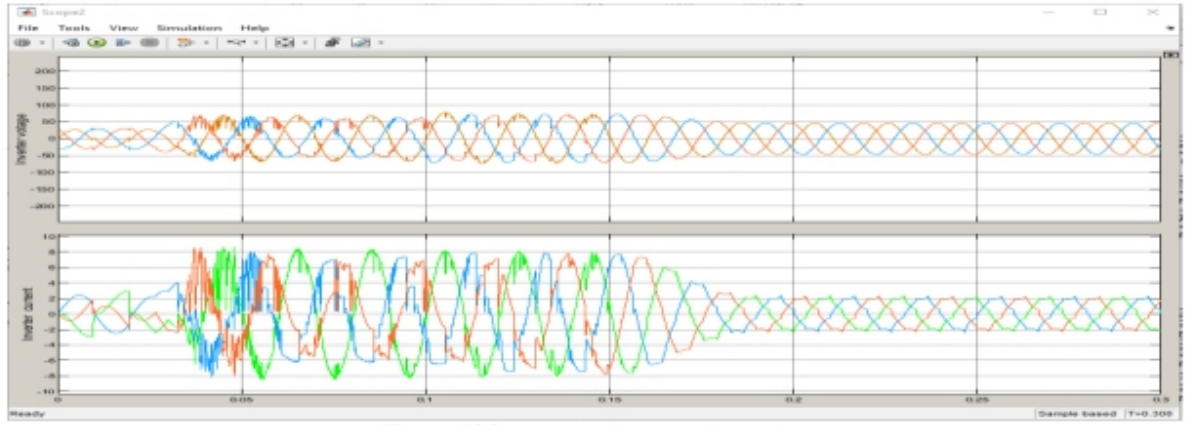

Figure 19 inverter voltage and current

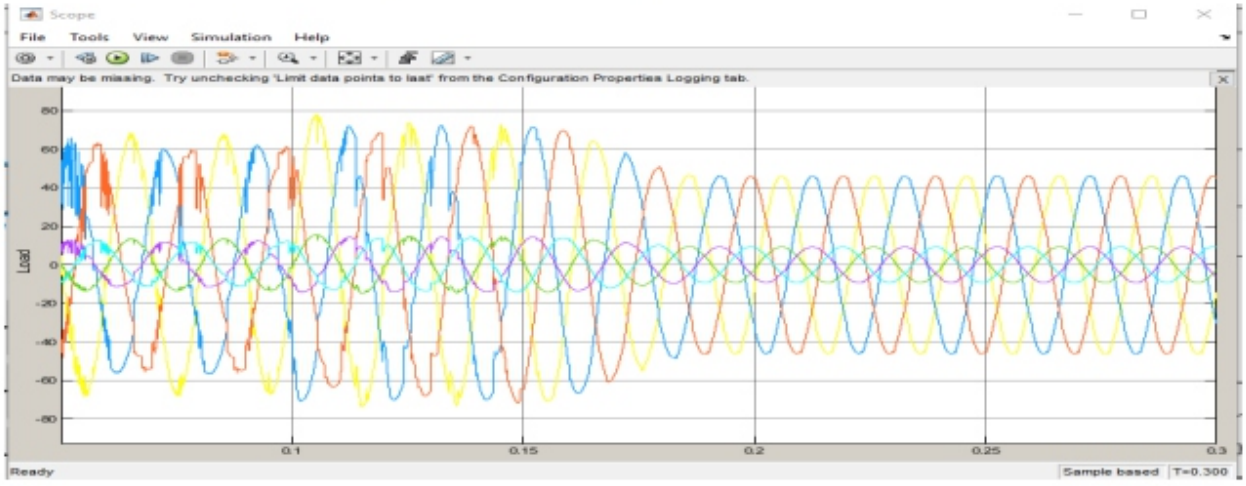

Figure 20 load voltage and current

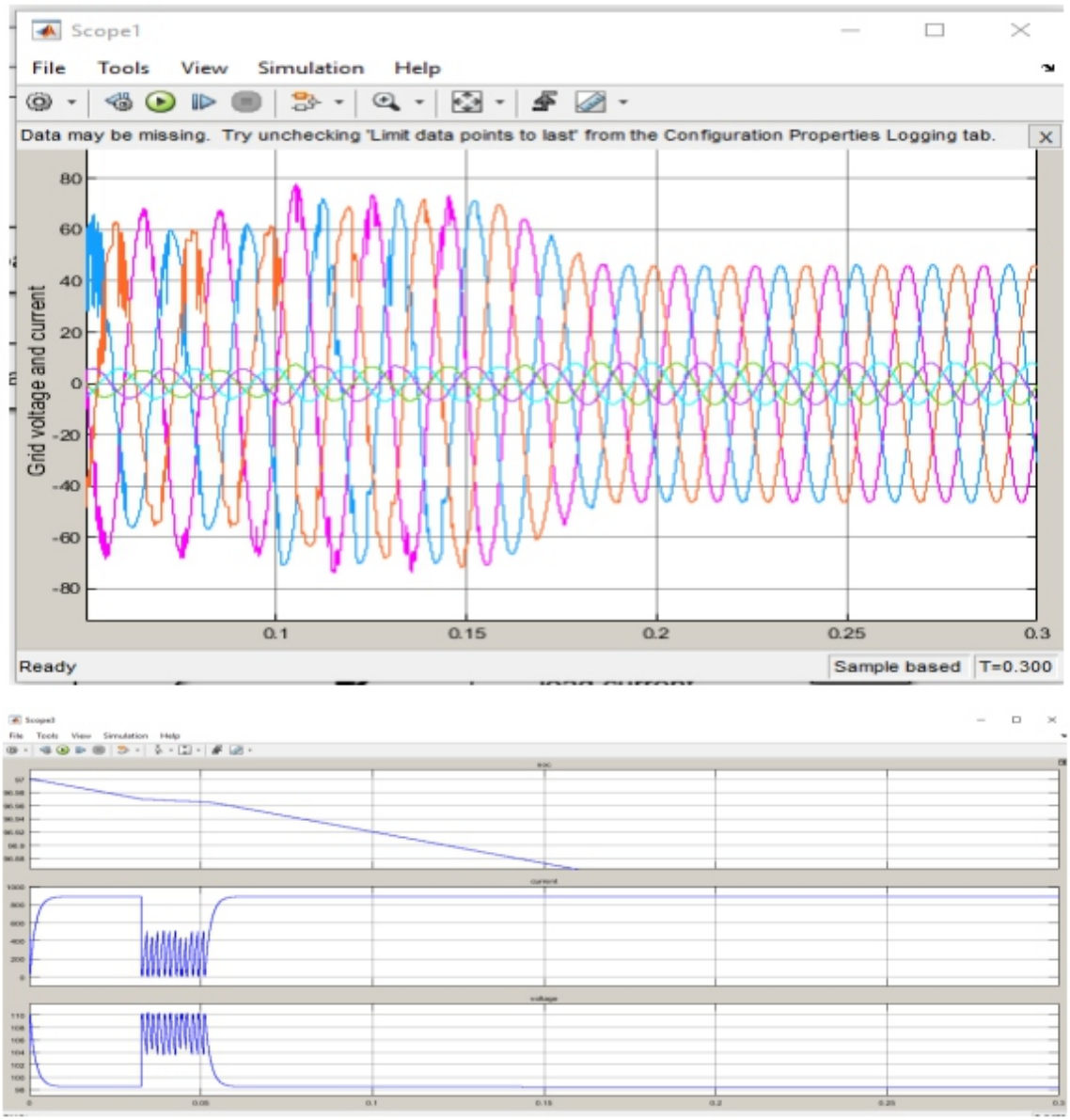

Figure 22 Battery Output

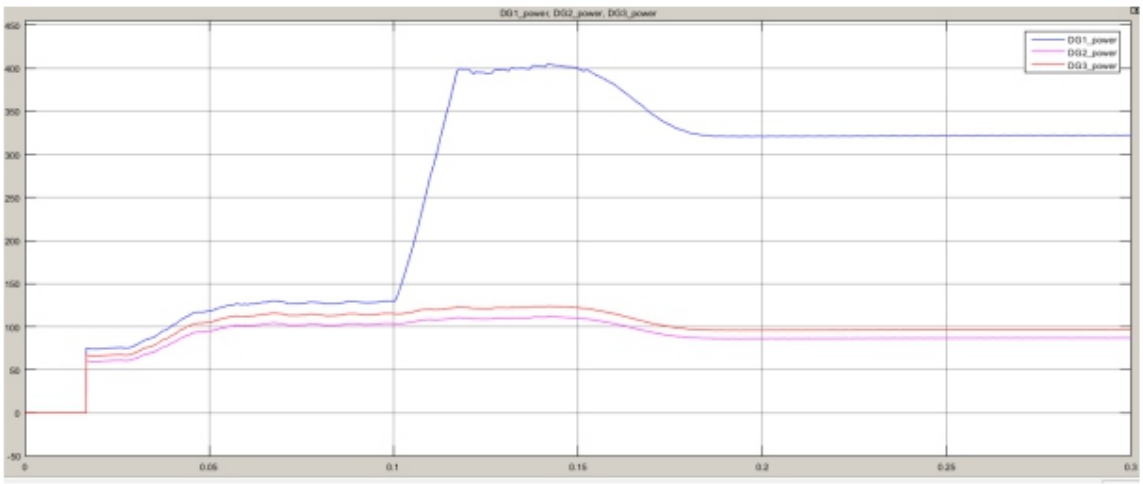

Figure 23 DG1, DG2, DG3 Power Output

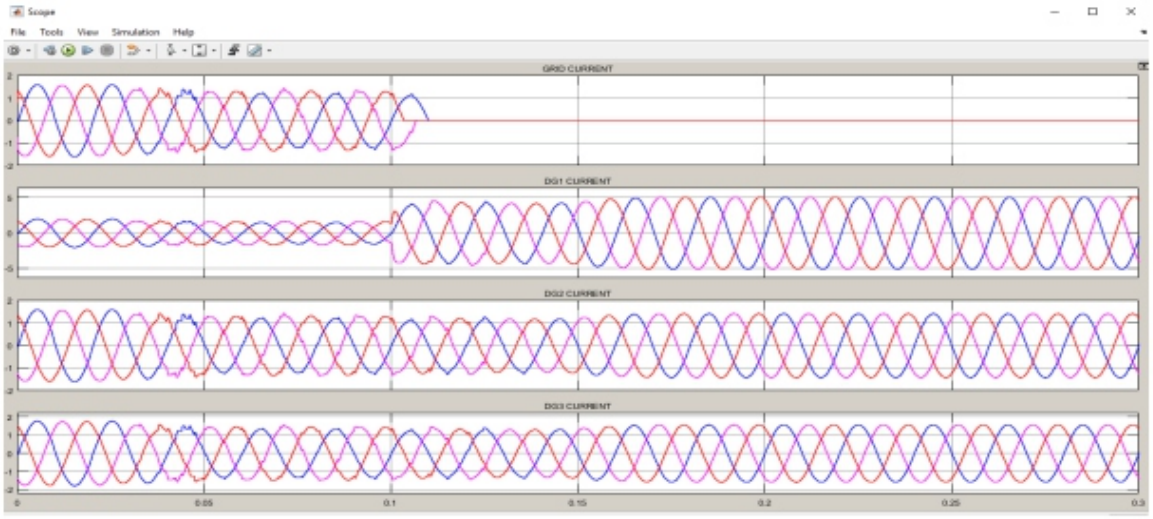

Figure 24 Grid Current, DG1, DG2, DG3 Output Current

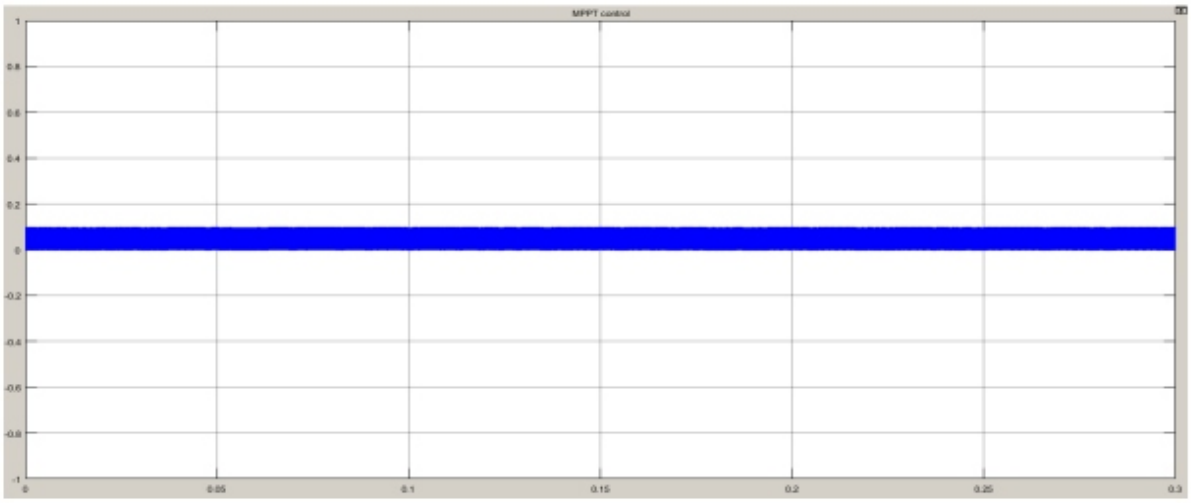

Figure 25 MPPT Control Output

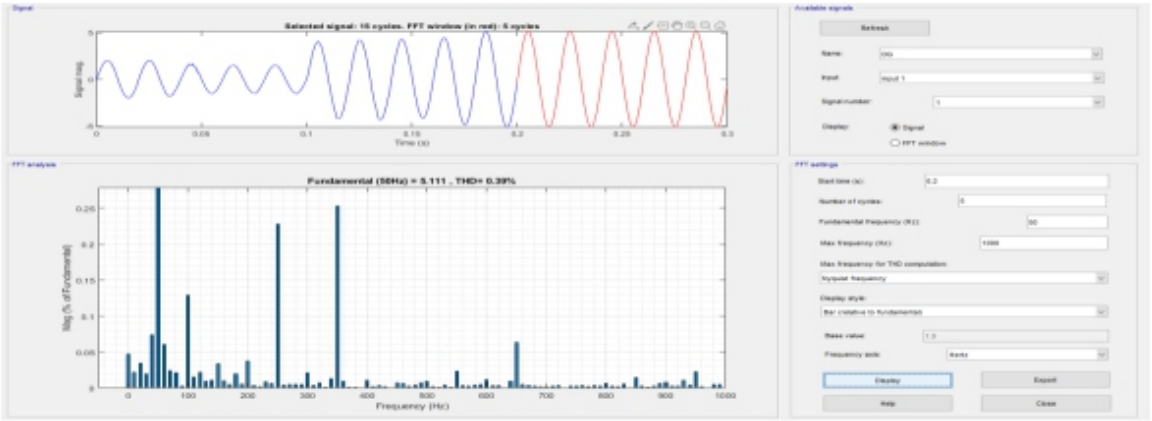

Figure 26 THD performance of perturb and observation MPPT

Power quality metrics were enhanced in the THD analysis conducted in a MATLAB/SIMULINK environment as a result of the hybrid-based grid integration system's overall performance. Table 2 displays the results of comparing the proposed MPPT method to the current MPPT method

Table 2 Comparison with existing work

Techniques	MPPT	THD
EXISTING TECHNIQUE	Fuzzy logic control	2.20%
PROPOSED TECHNIQUE	Perturb and observation	0.39%
	Incremental and conductance	0.44%

IV. CONCLUSIONS

Conventional energy resources have a substitute source in renewable energy. In far-off places where conventional energy cannot be delivered, renewable energy sources are the main ones available. This thesis investigates the MPPT based solar-wind hybrid energy system including boost converter. An MPPT algorithm is applied to raise the hybrid system's conversion efficiency. The necessary duty ratio to manage the boost converter under erratic weather circumstances is found via perturb and observe method and incremental behaviour. In this paper, a thorough investigation of solar, wind, and PMSG modelling has been undertaken. In terms of both dynamic and static performance, the simulation results show that the combination of the generator-side inverter controller, pitch angle controller, and grid-side inverter controller works quite well. The generator wind turbine may be operated efficiently by following the highest power setting. Keeping the DC-link voltage constant allows for decoupling management of the active and reactive power sources. In this way, the output will become the grid's optimal power source. Power storage devices, wind turbines constructed from permanent synchronous generators, and photovoltaic (PV) panels are also a part of the solar design. Using augmented conductivity technology, MPPT is applied to wind and photovoltaic energy systems. After MPPT, the PV array is linked to a DC-DC converter amplifier and subsequently to a standard bus network. The current fuzzy MPPT controller is compared to THD, incremental and conductance MPPT methods, and the suggested method in this virtual experiment. The suggested methods outperform the current ones in terms of THD. The continuous operation of power generating is affected by environmental factors and climatic fluctuations. To mitigate this, a hybrid PV-Wind model is suggested, as the production of a single renewable energy source is not enough to meet load demand. A boost converter to reduce inverter anomalies and an incremental based maximum power point tracking (MPPT) technique allow for effective tracking of solar energy. Power from wind turbines that use permanent magnet synchronous generators has a sinusoidal alternating current (AC) waveform. The grid is able to meet the demands by combining the two energy sources.

In the future, we want to apply optimization-based supreme power point tracking (MPPT) methods to solar, wind, and hybrid power generating systems in order to get the most power out of them and send it to the load. While the project is effective for continuous power generation, the total systems performance is affected by power quality difficulties. Voltage sag, voltage swell, harmonics, and transients are power quality concerns that primarily diminish the quality of power output from renewable sources like wind and solar.

Using more power-hungry electronics also affects the energy output, which causes variations. Static compensators and series-type LC filters (UPQC) are two methods that have shown promise in resolving power quality issues. Harmonic elimination, power factor correction, and load balancing are all made easier using DSTATCOM. Stability is ensured by utilising STATCOM. To estimate power for a continuous energy supply, modern ways of recording solar and wind data are required. The resources can be tracked using MPPT

REFERENCES

[1] R. H. Lasseter, "Microgrids," in 2002 IEEE Power Engineering Society Winter Meeting. Conf. Proc., vol. 1, 2002, pp. 305–308 vol.1.

[2] Y. Jia, R. Shibata, N. Yamamura, and M. Ishida, "Characteristics of smoothed-power output topology of stand alone renewable power system using edlc," in 2006 37th IEEE Power Electron. Specialists Conf., June2006, pp. 1–7.

[3] M. Hamzeh, A. Ghazanfari, Y. A. R. I. Mohamed, and Y. Karimi,"Modeling and design of an oscillatory current-sharing control strategy in dc microgrids," IEEE Trans. Ind. Electron., vol. 62, no. 11, pp. 6647–6657, Nov 2015.

[4] S.-T. Kim, S. Bae, Y. C. Kang, and J.-W. Park, "Energy management based on the photovoltaic hpcs with an energy storage device," IEEE Trans. Ind. Electron, vol. 62, no. 7, pp. 4608–4617, July 2015.

[5] N. R. Tummuru, M. K. Mishra, and S. Srinivas, "Dynamic energy management of renewable grid integrated hybrid energy storage system,"IEEE Trans. Ind. Electron., vol. 62, no. 12, pp. 7728–7737, Dec 2015.

[6] Yadav, M. and Singh, N., 2021. Small-signal modeling based hybrid optimized current and voltage controller for unbalanced DC microgrid. International Transactions on Electrical Energy Systems, 31(10), p.e12797.

[7] R. Dougal, S. Liu, and R. White, "Power and life extension of batteryultracapacitorhybrids," IEEE Trans. Compon. Package. Technol., vol. 25,no. 1, pp. 120–131, Mar 2002.

[8] S. K. Kollimalla, M. K. Mishra, and N. L. Narasamma, "Design and analysis of novel control strategy for battery and supercapacitor storage system," IEEE Trans. Sustain. Energy, vol. 5, no. 4, pp. 1137–1144, Oct2014

[9] U. Manandhar, N. R. Tummuru, S. K. Kollimalla, A. Ukil, G. H.Beng, and K. Chaudhari, "Validation of faster joint control strategy forbattery- and supercapacitor-based energy storage system," IEEE Trans.Ind. Electron, vol. 65, no. 4, pp. 3286–3295, April 2018.

[10]S. K. Kollimalla, M. K. Mishra, A. Ukil, and H. B. Gooi, "Dc gridvoltage regulation using new hess control strategy," IEEE Trans. Sustain.Energy, vol. 8, no. 2, pp. 772–781, April 2017.

[11]Shukla, A., Yadav, M. and Singh, N., 2019, September. Control and implementation of bi-directional converter for power management of unbalanced DC microgrid. In 2019 International Conference on Computing, Powerand Communication Technologies (GUCON) (pp. 343-349). IEEE.

[12]S. K. Kollimalla, A. Ukil, H. B. Gooi, U. Manandhar, and N. R.Tummuru, "Optimization of charge/discharge rates of a battery using atwo-stage rate-limit control," IEEE Trans. Sustain. Energy, vol. 8, no. 2,pp. 516–529, April 2017.

[13]H. Zhou, T. Bhattacharya, D. Tran, T. S. T. Siew, and A. M. Khambadkone,"Composite energy storage system involving battery and ultracapacitorwith dynamic energy management in microgrid applications,"IEEE Trans. Power Electron., vol. 26, no. 3, pp. 923–930, March 2011.

[14]D. Bazargan, S. Filizadeh, and A. M. Gole, "Stability analysis ofconverter-connected battery energy storage systems in the grid," IEEETrans. Sustain. Energy, vol. 5, no. 4, pp. 1204–1212, Oct 2014.

[15]Yadav, M. and Singh, N., 2022. Impact of variable negative solar resistance: modified virtual feed forwarded with feedback emulated inertia controller. International Journal of Ambient Energy, 43(1), pp.6511-6523.

[16]A. A. Radwan and Y. A. R. I. Mohamed, "Assessment and mitigationof interaction dynamics in hybrid ac/dcdistribution generation systems,"IEEE Trans. Smart Grid, vol. 3, no. 3, pp. 1382–1393, Sept 2012.

[17]D. Wang and F. Z. Peng, "Smart gateway grid: A dg-based residentialelectric power supply system," IEEE Trans. Smart Grid, vol. 3, no. 4,pp. 2232–2239, Dec 2012.

[18]M. Sechilariu, B. Wang, and F. Locment, "Building-integrated photovoltaicsystem with energy storage and smart grid communication," IEEETrans. Ind. Electron, vol. 60, no. 4, pp. 1607–1618, April 2013.

[19]Singh, S.K., Kumar, A., Jain, S., Singh, S., Narayan, E. and Yadav, M.R., 2024. Efficient MPPTmechanism for EVbatterycharging stationusingnovel hybrid optimization through cat-mouse and honey badger algorithms. Journal of basic science and engineering, 21(1), pp.2072-2099.

[20]S. Lee, G. Son, and J.-W. Park, "Power management and control for grid-connectedDGS with intentional islanding operation of the inverter," IEEETrans. Power Systems, vol. 28, no. 2, pp. 1235–1244, May 2013.

[21]Q. Xu, J. Xiao, P. Wang, X. Pan, and C. Wen, "A decentralizedcontrol strategy for autonomous transient powersharing and state-of-chargerecovery in hybrid energy storage systems," IEEE Trans. Sustain.Energy, vol. 8, no. 4, pp. 1443–1452, Oct 2017.

[22]Yadav, M.R. and Singh, N., 2023. Impact of negative solar resistance on DC microgrid stability: virtual damping voltage and current solar droop emulated controller. Journal of Circuits, Systems and Computers, 32(08), p.2350126

Representing Hierarchical Structured Data Using Cone Embedding

Daisuke Takehara and Kei Kobayashi

ALBERTInc., Shinjuku Front Tower 15F 2-21-1, Kita-Shinjuku, Shinjuku-ku, Tokyo 169-0074, Japan Department of Mathematics, Faculty of Science and Technology, Keio University, 3-14-1 Hiyoshi, Kohoku-ku, Correspondence:

ABSTRACT

Extracting hierarchical structure in graph data is becoming an important problem in fields such as natural language processing and developmental biology. Hierarchical structures can be extracted by embedding methods in non-Euclidean spaces, such as Poincaré embedding and Lorentz embedding, and it is now possible to learn efficient embedding by taking advantage of the structure of these spaces. In this study, we propose embedding into another type of metric space called a metric cone by learning an only one-dimensional coordinate variable added to the original vector space or a pre-trained embedding space. This allows for the extraction of hierarchical information while maintaining the properties of the pre-trained embedding. The metric cone is a one-dimensional extension of the original metric space and has the advantage that the curvature of the space can be easily adjusted by a parameter even when the coordinates of the original space are fixed. Through an extensive empirical evaluation we have corroborated the effectiveness of the proposed cone embedding model. In the case of randomly generated trees, cone embedding demonstrated superior performance in extracting hierarchical structures compared to existing techniques, particularly in high-dimensional settings. For WordNet embeddings, cone embedding exhibited a noteworthy correlation between the extracted hierarchical structures and human evaluation outcomes.

Keywords: *graph embedding; non-Euclidean space; WordNet*

Introduction

In recent years, machine learning methods for graph data have been an important topic, because graphs are suitable for representing the relation between multiple objects, such as social networks [1,2], links embedded in web pages [3], cells' interactions [4], and more. In particular, methods for extracting hierarchical structures from graph data are needed in fields such as cell engineering and natural language processing. Considering the structure of knowledge behind language is important for natural language processing tasks in general. The hierarchical structure of words provides useful information for improving the accuracy of question answering and semantic search [5,6]. In the field of developmental biology, various methods have been proposed for analyzing single-cell RNA sequence (scRNAseq) data to reveal the process by which an undeveloped cell develops into a cell with specific features [7]. Since scRNAseq data itself does not have a hierarchical structure, the hierarchical structure must be extracted from the data or from a graph constructed using the data. The methodforextracting hierarchical structures must have some scalability when it is applied to data sets with a large size and high dimensions such as scRNAseq data. The most common method for extracting the structure of a graph is to learn the embedding vector of nodes. Methods for learning node embeddings can be classified into two types: (1)

semi-supervised learning based on GNN [8–10] and (2) unsupervised learning [11] (based on random-walk [12], matrix factorization [13], and probabilistic methods [14], etc.). Graph neural networks (GNNs) are a type of neural network designed to operate on graph-structured data, allowing them to model complex relationships between entities, and capture both local and global information in the graph. This is achieved through the use of message passing mechanisms, which enable nodes to exchange information with their neighbors and aggregate that information into a new representation. Although it is possible to solve tasks that require hierarchical structure information using only GNNs, there are many advantages to using embedded representations, such as the expected reduction in computational complexity if the hierarchical structure is extracted in advance for embedding. On the other hand, the graph embedding converts each graph into a vector representing features of the graph and such vector representation can be tuned for solving individual tasks, which reduces the overall computational complexity. In this paper, we propose a novel graph embedding method for extracting its hierarchical structure from an undirected graph. There have been many graph embedding methods for extracting the hierarchical structure of a graph utilizing a hyperbolic space [15,16], such as Poincaré embedding [17–20], Lorentz embedding [21], and embedding in a hyperbolic entailment cone [22]. These methods use similar loss functions but with different metrics of the space in which graphs are embedded. Non-Euclidean spaces with non-zero curvature can learn embedding efficiently by adjusting their curvature to the hierarchically structured data. In particular, a Poincaré ball is a space of a negative constant curvature, which is characterized by the fact that the length of the circumference exponentially increases in the order of the radius when centered at the origin. An efficient embedding of tree-structured data utilizing this feature has also been proposed [23]. The Lorentz model of a hyperbolic space can explicitly describe geodesics and the accuracy of distance calculation becomes stable in the optimization [21]. The metric cone used as the embedding space in this study is a space defined as a one-dimensional extension of a base metric space. The base metric space can be not only a vector space but for any geodesic metric space such as Riemannian manifolds and metric graphs. The dimensions of the metric cone are only one dimension higher than the original space. It is known that the curvature of this space can be varied and a method of changing the structure of the data space for analysis has also been proposed [24]. The definition and details of the metric cone will be explained in Section 2.3. In this paper, we propose the use of the metric cone as an embedding method for hierarchical graphs. Thanks to the properties of metric cones, the proposed method has the following five advantageous features compared to existing methods. First, it optimizes an only one-dimensional coordinate corresponding to "the height of the metric cone" (a one-dimensional parameter added to the base space) as an indicator of hierarchy. Therefore, a significant reduction in computational complexity can be expected compared to optimizing all variables. Secondly, it can be applied to any pre-trained embeddings using a geodesic metric space including the Poincaré ball and the Lorentz model. When extracting hierarchical information for another purpose from an embedding already learned by other embedding methods, the

extraction of hierarchical structure can be accomplished by learning only one additional coordinate variable. Due to this scalability, the proposed method can be combined with various existing embedding methods to achieve hierarchical extraction with a variety of features. Thirdly, the curvature of embedding space varies monotonically with , a parameter in the distance function of embedding space, and therefore can be tuned by it. As explained in Section 3.2, parameter corresponds to the generatrix of the metric cone and this fact provides an intuitive explanation for the monotonically decreasing curvature of the embedding space as the parameter is increased; while there have been some methods for tuning the curvature of some graph embedding spaces [25,26], the metric cone allows the curvature of the space to be tuned by changing while keeping the coordinates of the original space fixed. Therefore, when adjusting the curvature of the embedding space to match the training data, only one-dimensional parameters need to be learned. As shown in the experiments, it is suitable to embed data with a smaller curvature in higher dimensions. Thus, it is important to adjust curvature depending on the dimension of the destination space and the structure of the data to be embedded. Fourthly, the uniqueness of the embedding is guaranteed when optimizing the loss function. When performing graph embedding in a space where isometric transformations exist, there is the problem of unstable learning due to the existence of multiple embeddings such that the distance from the origin of each point can be different, even though the distances between all points are identical. Usually, the distance from the origin is used as the height of the hierarchy, resulting in multiple solutions with different hierarchical structures. On the other hand, since there is no isometric mapping for a sufficiently large number of points in a metric cone as proven in Section 3.1, it is theoretically guaranteed that the embedding is unique and the learning is stable. Lastly, we can reduce the amount of computation for the parts other than preprocessing, regardless of the dimension. In addition, because the embedding in the original Euclidean space is preserved, it can be used as an input to the neural network and can be easily applied to other tasks. The subsequent sections of this paper are organized as follows. First, in Section 2, wepropose the method of graph embedding in a metric cone, with the introduction of (1) graph embedding in non-Euclidean spaces, and (2) the definition and properties of cones. In Section 3, theoretical arguments ensure the validity of the proposed method. First, weprove that the identifiability of the graph embedding, which does not hold for existing methods, holds for the cone embedding. Next, we show that the curvature of the metric cone varies monotonically with the parameter . In Section 4, we present experimental results using some real and artificial graph data, followed by a conclusion and future perspectives in Section 5.

2. Methods

2.1. Problem Settings

From this point onward, the set of edges in an undirected graph G is denoted by E, the set of vertices by V, and the embedded space by X. Then, our target is finding an embedding : V Xandafunctionh : X Rsuchthath((v))representsthehierarchy of v V.Function h canusually be expressed simply as a coordinate value of X. Note that, since G is an undirected graph, the problem is ill-posed if there are no

assumptions about the relationship between the structure of the graph and the hierarchy of vertices. As in existing works, we implicitly assume that the branching of the graph is like that of a rooted tree, i.e., the higher the hierarchy, the smaller the number of vertices, and the lower the hierarchy, the more vertices.

2.2. Graph Embedding in Non-Euclidean Spaces

Out learning steps are similar to Poincaré embedding. We learn the embedding of a graph G bymaximizing the following objective function:

$$L = \sum_{(u,v)\in E} \log \frac{\exp(-d(u,v))}{\sum_{v'\in N^c(u)} \exp(-d(u,v'))}, \tag{1}$$

where $N^c(u) : \{v' \in V|(u,v') \notin E\}$ denotes the set of points not adjacent to node u (including u itself) and d denotes the distance function of the embedded space. Here the embedded space becomes a Poincaré sphere for the Poincaré embedding and a metric cone for the proposed method. This objective function is a negative sampling approximation of a model in which the similarity is -1 times the distance and the probability of the existence of each edge is represented by a SoftMax function on the similarity.

The maximization of the objective function is done by stochastic gradient descent on Riemannian manifolds (Riemannian SGD). The stochastic gradient descent over Euclidean space updates the parameters as follows:

$$u \leftarrow u - \eta \nabla_u L(u), \tag{2}$$

where η is the learning rate. However, in non-Euclidean, the sum of vectors is not defined and $\nabla_u L(u)$ is the point of the tangent space $T_u X$ of u; hence, SGD cannot be applied. Therefore, we update the parameters by using an exponential map instead of the sum:

$$u \leftarrow \exp_u(-\eta \nabla_u^R L(u)). \tag{3}$$

With the metric tensor of the embedding space as $g_u(u \in V)$, the gradient on the Riemannian manifold $\nabla_u^R L(u)$ is the scaled gradient in Euclidean space:

$$\nabla_u^R L(u) = g_u^{-1} \nabla_u L(u). \tag{4}$$

2.3. The Metric Cone

The metric cone is similar to ordinary cones (e.g., circle cones) in the sense that it is defined as a collection of line segments connecting an apex point to a given set. However, the metric cone has a notable property such that every point in the original set is embedded

at an equal distance from the apex point and this is a desirable property for hierarchical structure extraction. The metric cone has been studied as an analogy to the length metric spaces of the tangent cone for differential manifolds with singularities. Length metric space is a metric space where the distance between any two points is equal to the shortest curve length connecting them. Length metric space includes Euclidean spaces, normed vector spaces, manifolds (e.g., Poincaré ball; sphere), metric

metric cone generated by Z is X := Z [0,1] / Z 0 with a distance function determined as follows:

$$\tilde{d}_\beta((x,s),(y,t)) = \beta\sqrt{t^2+s^2-2ts\cos(\pi\min(d_Z(x,y)/\beta,1))} \quad (5)$$

where $\beta > 0$ is a hyperparameter corresponding to the length of the conical generatrix. Note that the metric cone itself also becomes a length metric space and it embeds the original space (i.e., the space is one dimension larger than the original space). The distance in the metric cone corresponds to the length of the shortest curve on the circle section (blue line segment(s) in the right two subfigures in Figure 1) whose bottom circumference is the distance of the original space Z and whose radius is β.

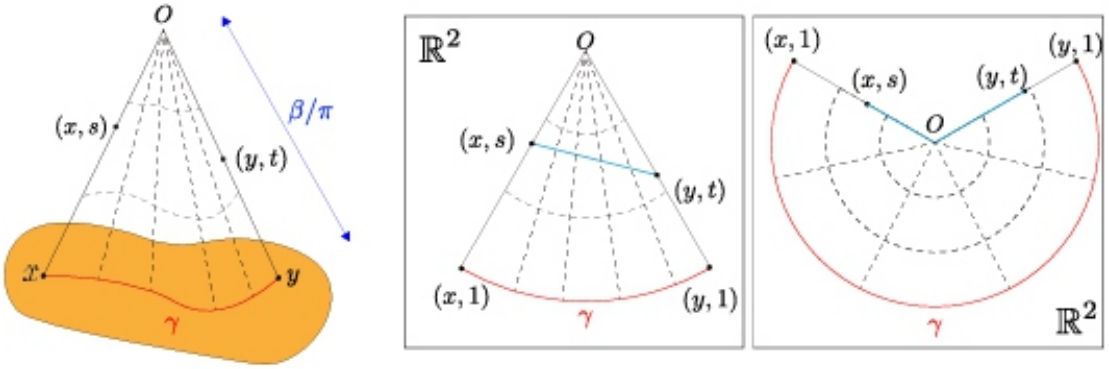

Figure 1. The left figure depicts a conceptual image of an original space and its metric cone. A circle section to compute the distance in the metric cone is depicted in the middle figure (when the apex angle $< \pi$) and the right figure (when the apex angle $\geq \pi$).

When the curvature is measured in the sense of CAT(k) property, a curvature measure for general length metric spaces, the curvature value k can be controlled by β. Other properties of the metric cone are examined in [27,28]. Because the metric cone can change the curvature of the space by changing parameter β, its usefulness has been reported in an analysis using the structure of the data space [24].

The metric $\tilde{g}$ of a metric cone is obtained by calculating the two-time derivative of the distance as follows (see Appendix A for more details):

$$\tilde{g}_{(x,s)} = \begin{pmatrix} \pi^2 s^2 g_x & 0 \\ 0^\top & \beta^2 \end{pmatrix}, \quad (6)$$

where g_x represents the metric of Z at x. Combining this metric and the argument in Section 3.1, the algorithm of cone embedding can be described as Algorithm 1.

Algorithm 1 Learn the cone embedding $\{(u,s)\}$

Input: graph $G = (V,E)$, cone's hyperparameter β , learning rate η, and the pre-trained embedding $\{x\}$ in original space Z

Output: the cone embedding $\{(u,s)\}$

1: calculate the distance matrix $D = (d_{ij})$, $d_{ij} = d_Z(x_i, x_j)$

2: minimize the softmax loss function:
(calculate efficiently by referencing the distance matrix D)

$$L = \sum_{((u,s),(v,t))\in E} \log \frac{\exp^{-\tilde{d}_\beta((u,s),(v,t))}}{\left(\sum_{(v',t')\in N^c((u,s))} \exp\left(-\tilde{d}_\beta((u,s),(v',t'))\right)\right)} \tag{7}$$

via Riemannian stochastic gradient descent:

$$(x,s) \leftarrow \mathrm{proj}\left((x,s) - \eta \bar{g}^{-1} \nabla L\right)$$

The loss function (7) is defined to be smaller if the distance between nodes sharing an edge becomes smaller (by the numerator in the log) and the distance between nodes without an edge becomes larger (by the denominator in the log). Note that the distance for a metric cone is used here. Computation of the denominator can be reduced by random sampling of nodes for which no edges exist. Furthermore, the projection normalizes the embedding along the gradient so that it does not jump out of the metric cone when it is updated.

Instead of the exponential map of the metric cone, we use the first-order approximation using $\mathrm{proj}(x,s)$:

$$\mathrm{proj}(x,s) = \begin{cases} (x,s) & \text{if} \quad \epsilon < s < 1-\epsilon, \\ (x,1-\epsilon) & \text{if} \quad s \geq 1-\epsilon, \\ (x,\epsilon) & \text{if} \quad s \leq \epsilon. \end{cases} \tag{8}$$

2.4. Score Function of Hierarchy

The Poincaré embedding defines an index in [17], which is aimed to be an indicator of the hierarchical structure and depends on the distance from the origin:

$$\mathrm{score}(u,v) = -\alpha(\|v\| - \|u\|)d(u,v) \tag{9}$$

This score function is penalized by the part after α, so, if v is closer to the origin than u, then it is easier to obtain larger values. In other words, v is higher in the hierarchy than u (i.e., "u is a v" relationship holds). However, it is not appropriate to use this indicator for the Poincaré embedding. This model learns the embedding by maximizing (1), where

$$d(x,y) := \mathrm{arcosh}\left(1 + \frac{\|x-y\|^2}{(1-\|x\|^2)(1-\|y\|^2)}\right). \tag{10}$$

This loss function only depends on the distance between the two embeddings. However, an isometric transformation in the Poincaré ball exists, known as the Möbius transformation [29]. Möbius transformation is defined as a map $f : \mathbb{B}^n(\text{open unit ball}) \to \mathbb{B}^n$, which can be written as a product of the inversions of $\bar{\mathbb{R}}^n (:= \mathbb{R}^n \cup \{\infty\})$ through a sphere S that preserves $\mathbb{B}^n$.

In contrast to the Poincaré ball, the isometric transformation on the metric cone does not exist when the coordinate in the original space is fixed (we prove this property in Appendix C). When we embed a graph into a metric cone, we define an indicator of the hierarchical structure by replacing the norm with a coordinate corresponding to the height of the cone (a one-dimensional parameter added to the original space):

$$\mathrm{score}((\mathbf{u},s),(\mathbf{v},t)) = -\alpha(s-t)d(\mathbf{u},\mathbf{v}). \tag{11}$$

A point closer to the top of the cone is higher in the hierarchy, which is natural for representing hierarchical structure.

2.5. Using Pre-Trained Model for Computational Efficiency and Adaptivity for Adding Hierarchical Information

Consider a situation where we already have a trained graph embedding on a Euclidean space (e.g., LINE [14]) and we try to learn the embedding in a metric cone of Euclidean space to extract information about the hierarchical structure. In this case, we can reduce the computational cost by fixing the coordinates corresponding to the original Euclidean space and learn only the one-dimensional parameters corresponding to heights in a metric cone added to the original space because the metric cone is one dimension larger than the original space. The distance between each embedding in the original space is calculated beforehand, since no updates are made by learning except for the 1D parameter to be added. By referring to the pre-computed distances in the original space when calculating the distances between each embedding on the metric cone ($d_z(x, y)$ in Equation (5)) during training, we can reduce the amount of computation for the parts other than preprocessing, regardless of the dimension. In addition, because the embedding in the original Euclidean space is preserved, it can be used as an input to the neural network (when the task considers information about the hierarchy and the added one-dimensional parameters are also used as input) and can be easily applied to other tasks. However, other non-Euclidean embedding methods to extract hierarchical structures are not scalable because these methods cannot be applied directly to solve other tasks. For example, deep neural networks cannot use a non-Euclidean embedding as input because the sum of two vectors in the space and scalar product is not generally defined.

2.6. Comparison with Hierarchical Clustering

Although both cone embedding and hierarchical clustering aim to extract hierarchical structures, there is a clear difference between their problem settings. In hierarchical clustering, only leaves in a result tree (dendrogram) correspond to data points and other nodes correspond to created clusters. Thus, the problem setting differs significantly from cone embedding in which each node in a data graph corresponds to a pre-defined entity. As a result, hierarchical clustering cannot extract the hierarchy of nodes other than leaves while cone embedding can do. Moreover, the order of computational complexity is also different: hierarchical clustering requires $O(n^2)$, while cone embedding requires $O(|E|)$ ($|E|$: number of edges), making it suitable for extracting hierarchical structures in large graphs.

It has been also shown by [30] that the embedding of tree-structured (undirected) graph data can be done naturally in hyperbolic space, but graph data with hierarchical structure does not necessarily have a tree structure in general (e.g., there can be a cycle when a child node has two parents which have the same parent). Thus, the combination with hyperbolic embedding and hierarchical clustering may not be suitable in such cases. Cone embedding does not assume the tree structure and extracts the hierarchical structure by using the property that the closer to the origin O the shorter the distance between data points, so that embedding can be learned even in this situation.

3. Theory

In this section, we give theoretical proof as to why the spatial properties of the metric cone are suitable for extracting hierarchical structures.

3.1. Identifiability of the Heights in Cone Embedding

As mentioned above, for Poincaré embedding, there is an isometric transformation on the Poincaré ball and the heights of the learned hierarchy are not invariant to such transformation. Here, we show that such a phenomenon does not occur for the cone embedding, i.e., the heights of the hierarchy are (almost) uniquely determined from the distance between the embedded data points in a metric cone.

Let Z be an original embedding space (connected length metric space) and let X be a metric cone of Z with a parameter $\beta > 0$. We assume that each data point $z_i \in Z$ $(i = 1, \dots, n)$ has its specific "height" $t_i \in [0, 1]$ in the metric cone X. Our proposed method embeds data points into a metric cone based on the estimated distances $\tilde{d}_\beta(x_i, x_j)$ $(i, j = 1, \dots, n)$ and tries to compute the heights $t_1, \dots, t_n$ as a measure of the hierarchy level. However, it is not evident whether these heights are identifiable only from the information of the original data points in Z and the distances $\tilde{d}_\beta(x_i, x_j)$ $(i, j = 1, \dots, n)$ in the metric cone. The following theorem guarantees some identifiability. (A rigorous version of Theorem 1, including the precise meaning of "identifiable" in (a)–(c) and "general" in (b), is explained in Appendix C.)

Theorem 1. *(a) Let $n \geq 3$ and assume that $z_1, \dots, z_n$ are not all aligned on a geodesic in Z. Then, the heights $t_1, \dots, t_n$ are identifiable up to at most four candidates.*

(b) Let $n \geq 4$ and assume $z_1, \dots, z_n$ and $t_1, \dots, t_n$ take "general" positions and heights, respectively. Then, the heights $t_1, \dots, t_n$ are identifiable uniquely.

(c) If $d_Z(z_i, z_j) \geq \frac{\beta}{2}$ for all $i, j = 1, \dots, n$, $i \neq j$, then the heights $t_1, \dots, t_n$ are identifiable uniquely.

Theorem 1(a) indicates that the candidates of heights are finite and we can expect the algorithm to converge to one of them, except for a very special data distribution in the original space Z. Moreover, by (b), even the uniqueness can be proved under very mild conditions. The statement in (c) implies that the uniqueness holds for arbitrary data distributions when we set β sufficiently small.

Remark that the assumption of "general" positions in Theorem 1(b) is satisfied easily for most data distributions. For example, if both $z_1, \dots, z_n \in \mathbb{R}^d$ and $t_1, \dots, t_n \in [0, 1]$ are i.i.d. from a probability distribution whose density function exists with respect to the Lebesgue measure, then it is easy to see the assumption holds almost surely and therefore the uniqueness of the solution is guaranteed. Note that, for $n = 3$ under the same setting, there can be multiple solutions with a positive probability.

3.2. Variable Curvature

One of the essences of Poincaré embedding is that a negative curvature of the Poincaré sphere is suitable for embedding tree graphs. The curvature of a metric cone has a similar property, i.e., a metric cone has more negative curvature than the original space and, furthermore, the curvature can be controlled by hyperparameter β. We will verify these facts mathematically from two different aspects: (i) the scalar and the Ricci curvatures of a Riemannian manifold and (ii) the CAT(k) property of a length metric space.

First, assume the original space $\mathcal{M}$ is an n-dimensional Riemannian manifold with a metric g. Then the metric $\tilde{g}$ of the corresponding metric cone with β can be defined except for the apex and it becomes as (6). Let $1, \dots, n$ be coordinate indices corresponding to $x \in \mathcal{M}$ and 0 be the index corresponding to $s \in [0, 1]$. The Ricci curvatures $\tilde{R}_{ij}$ and the scalar curvature $\tilde{R}$ at (x, s) become

$$\tilde{R}_{\alpha\gamma} = R_{\alpha\gamma} - \pi^2(n-1)\beta^{-2}\tilde{g}_{\alpha\gamma}, \tag{12}$$
$$\tilde{R}_{\alpha 0} = \tilde{R}_{0\alpha} = \tilde{R}_{00} = 0, \tag{13}$$
$$\tilde{R} = \{\pi^{-2}R - n(n-1)\beta^{-2}\}s^{-2} \tag{14}$$

where α, γ are coordinate indices in $1, \ldots, n$ and R_{ij} and R are the Ricci curvatures and the scalar curvature of $\mathcal{M}$, respectively. See Appendix B for the derivation of such curvatures. The scalar curvature and the Ricci curvatures $\tilde{R}_{\alpha\gamma}$ become more negative than (a constant times of) the original curvature for $\beta < \infty$ and $n \geq 2$. Moreover, the smaller value of β makes the curvature more negative; thus, it becomes possible to control the curvature by tuning β. Note that, the closer to the apex, i.e., the smaller the value of s, the greater the change of the scalar curvature.

Second, assume the original space $\mathcal{M}$ is a length metric space. This does not require a differentiable structure and is more general than the Riemannian manifold. In this case, we cannot argue the curvatures using the Riemannian metric but the CAT(k) property can be used instead. In [24], they proved the curvature of the metric cone is more negative or equal to the curvature of the original space and it can be controlled by β in the sense of the CAT(k) property.

4. Experiments

The claim in this paper is that "a hierarchical structure can be captured by adding a one-dimensional parameter and embedding it in a metric cone." Therefore, we evaluate the proposed method in two experiments:

- Prediction of edge direction for artificially directed graphs;
- Estimation of the hierarchical score by humans for WordNet.

As a comparison, we compare the proposed method with two other methods: Poincaré embedding [17] and ordinary embedding in Euclidean space, which are known to capture the hierarchical structure of graphs. For Euclidean embedding, we use the distance from the mean of embedded data points as the hierarchical score in (8).

4.1. Prediction of Edge Direction for Directed Graphs

In this experiment, we estimate the orientation of directed edges for some simple graphs such that it is natural to think of the direction of the edges as representing the vertical relationship in the hierarchy.

4.1.1. Settings

We use the following three patterns of graphs with a naturally set hierarchical structure:

- Graphs generated by a growing random network model called the Barabási–Albert preferential attachment [31] with $m = 2$, where m is the number of edges to attach from a new node to existing nodes;
- Complete k-ary tree;
- Concatenated tree of two complete k-ary sub-trees.

For the growing random network model, the hierarchy and the corresponding orientation is naturally defined by the order in which each node is attached. For each tree, node depth can be treated as its hierarchy. The concatenated tree is created by connecting the roots of two complete k-ary trees to a new node, which is then used as the new root. The concatenated tree is considered to study the effect of node degree on the cone embedding as will be explained below.

In this experiment, we learn the embedding of each directed graph. However, we use the information of directions only for evaluation and not for learning. For each directed edge of the learned graph, we estimate the direction by the computed hierarchical scores $score(u, v)$:

$$\text{total\_score} = \sum_{(u,v)\in E} s\tilde{c}ore(u, v)/|E| \tag{15}$$

$$s\tilde{c}ore(hypo, hype) = \begin{cases} 1 & score(hypo, hype) > 0 \\ 0 & \text{otherwise} \end{cases} \tag{16}$$

where $hype$: higher hierarchy node

$hypo$: lower hierarchy node

Hyperparameters were set as follows. First, the number of negative samplings was set to 5; while increasing the number of negative samplings increases the amount of computation, the effect on accuracy was not significant, so it was set small. Learning was performed for values of β at 0.1, 0.5, 1, and 5, and the best results are described in Table 1. Here all nodes and edges of the graph are used for both training and evaluation.

Table 1. Result for prediction of edge direction for directed graphs. (We list accuracy and standard deviation. Compared to other methods, cone embedding tends to extract the hierarchical structure correctly even when the number of nodes increases).

Model	Barabási–Albert (Nodes: 100)	Complete k-Ary-Tree		Concatenated k-Ary Trees	
		k = 3 (121)	k = 5 (781)	k = 3 (81)	k = 5 (313)
Cone	0.936 (sd: 0.005)	0.787 (0.049)	**0.799** (0.037)	0.783 (0.045)	**0.744** (0.056)
Euclidean	0.181 (0.004)	0.074 (0.088)	0.127 (0.020)	0.190 (0.136)	0.155 (0.031)
Poincaré	**0.957** (0.012)	**0.935** (0.015)	0.351 (0.022)	**0.880** (0.060)	0.606 (0.043)

4.1.2. Results

The experimental results are shown in Table 1 and the cone embedding shows overall good and stable estimation accuracy for hierarchies. Examples in Figure 2 depict how each graph is embedded in a metric cone. Other existing methods may outperform for sparse trees (small degree of each node) but this method has an advantage for dense trees. The reason for the instability in the accuracy of Poincaré embedding may be the lack of invariance with respect to the equidistance transformation, as we have explained. The main reason for the poor hierarchical estimation accuracy of Euclidean embedding is that the root or higher hierarchical nodes are embedded apart from the cluster of other nodes as in Figure 3. As a result, the root node becomes far from the origin of the embedded space.

For the Barabási–Albert model, the relationship between the (added 1D) coordinates of the cone hierarchy and the order is shown in Figure 4. We can see that there is a strong relationship between the degree and the hierarchy. This raises the suspicion that the degree of the node alone determines the hierarchy of the embedding. However, the fact that the cone embedding provides high estimation accuracy even for the concatenated trees with low root degree indicates that this is not true.

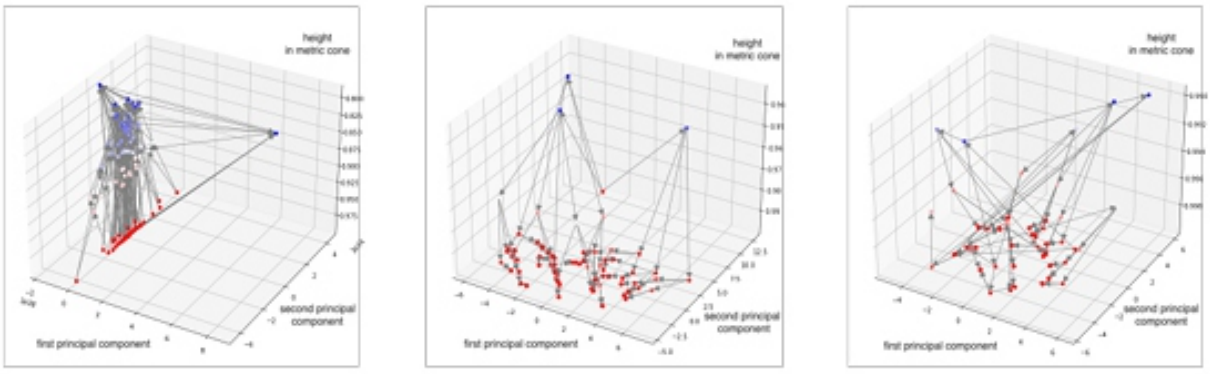

Figure 2. Graphs used for training: (**left**) model trained by Barabási–Albert model, (**middle**) complete k-ary tree, (**right**) concatenated tree of two complete k-ary trees. The x- and y-axes represent embedding in Euclidean space, which is dimensionally reduced to two dimensions by principal component analysis, and the z-axis represents the height in the metric cone (coordinates representing the hierarchy).

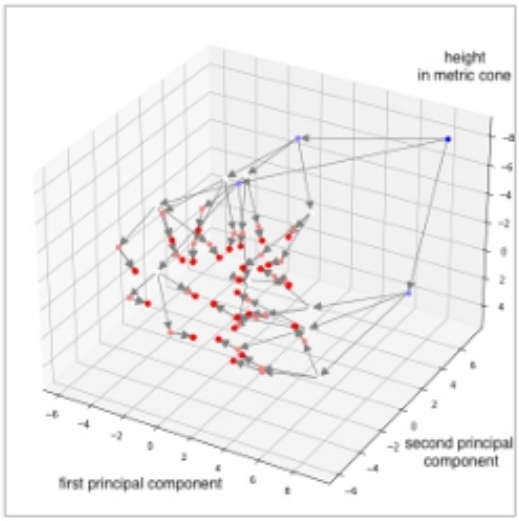

Figure 3. An embedding of the complete k-ary tree ($k = 3$). Each point is plotted by the 3D Euclidean embedding and the color represents length of shortest path from root node (the bluer the color, the higher the hierarchy).

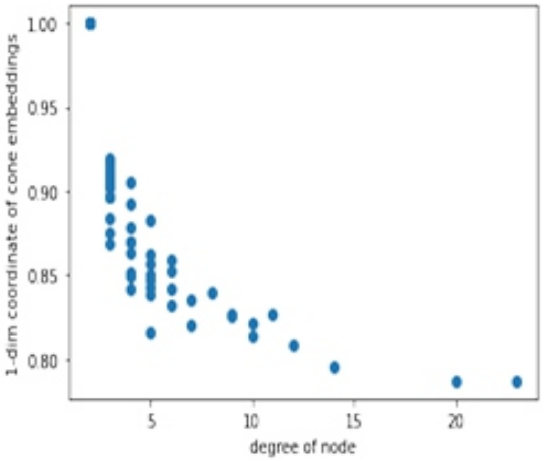

Figure 4. Plot of the hierarchy value of each node in a cone embedding (a newly added one-dimensional parameter) against their node degree.

4.2. Embedding Taxonomies

Following an experiment in [17] for the Poincaré embedding, we evaluate the embedding accuracy of the hierarchical structure using WordNet. To verify this, we embed the nouns in WordNet into a metric cone and use the score function ("total_score" described in Section 4.1). Note that hyperparameter α was set to 10^3. The output of this score function and the correlation coefficient of the HyperLex dataset's score (evaluated manually whether a word is a hyponym of another word) are used to evaluate the ability to represent the hierarchical structure of the model.

In addition to hierarchical scores, we also evaluate the accuracy of graph embedding. We use mean rank and mean average precision, which are commonly used in existing graph embedding accuracy, as evaluation metrics. The mean rank is calculated for each node as the rank of its neighbors when sorted in order of distance. The mean average precision is calculated as follows:

1. Fix one node and calculate the distance to all other nodes.
2. Consider the node adjacent to the fixed node as the correct data, and calculate the average precision for this correct data using the distance as the confidence score.
3. Perform the above two operations on all the nodes and take the average.

The embedding accuracy (mean rank (MR) and mean average precision (MAP)) and correlation coefficients are also shown in Table 2. Note that all of the graph data are used for training and the results are evaluated according to the accuracy with which the graph is reconstructed from the learned embedding. Because the same data are used for training and evaluation, we evaluate the fittingness of the embedding method to the data.

Table 2. MAP, mean rank (MR), Hyperlex score (correlation efficient) and computation time for WordNet. Cone embedding is trained from Euclidean embedding, e.g., in 10-dims cone embeddings, we trained additional 1-dim parameters from 10 dims Euclidean embeddings. For MR and comp. time lower is better, and for MAP and corr. higher is better.

Model	Evaluation Metric	Dimensions			
		10	20	50	100
Euclidean	MR	1681.18	583.75	233.7	162.43
	MAP	0.07	0.12	0.25	0.37
	corr	0.25	0.34	0.38	0.39
	comp. time	976.48	984.72	2169.1	2095.7
Poincaré	MR	1306.22	1183.29	1112.42	1096.08
	MAP	0.09	0.13	0.14	0.16
	corr	0.07	0.08	0.09	0.09
	comp. time	2822.99	1807.73	3954	2241.7
Cone	MR	**426.75**	675.09	777.3	910.51
($\beta = 1.0$)	MAP	**0.10**	0.08	0.07	0.06
	corr	**0.39**	**0.40**	**0.40**	**0.40**
	comp. time	177.94	174.67	**168.33**	**187.83**
Cone	MR	688.85	**143.23**	**74.39**	**51.32**
($\beta = 5.0$)	MAP	0.07	**0.23**	**0.50**	**0.57**
	corr	0.35	0.35	0.37	0.38
	comp. time	**176.04**	**171.21**	168.7	189.89

The table shows that our proposed model improves the score and captures the hierarchical structure better than other embedding methods. Furthermore, "comp. time" represents the time taken to train the embedding (1000 epochs); for cone embedding, it represents the time taken to train in one additional dimension (100 epochs). From the table, we can see that our method is efficient in learning and does not vary with the dimension of the embedding. The result also shows that the optimal β value can depend on the dimension. Because larger β corresponds to smaller curvature, the proposed method seems to perform better when embedding in a smaller curvature space if the dimension becomes higher. For the same reason, Euclidean embedding is considered to perform better than Poincare embedding in high dimensions due to their zero curvature. Tuning of β is necessary because the optimal value also varies depending on the training data. In this case, the search was done in $\beta = 0.1, 0.5, 1.0, 5.0$ but a finer search may improve the accuracy.

Furthermore, an example visualization of the hierarchical structure of the embedding vectors obtained by the training is shown in Figure 5. As the figure illustrates, the closer the coordinate corresponding to the height in the cone is to zero (closer to the top of the cone), the higher the noun in the hierarchy is located in the embedded representation. For visualization, the embedding vectors in Euclidean space were reduced to two dimensions by principal component analysis.

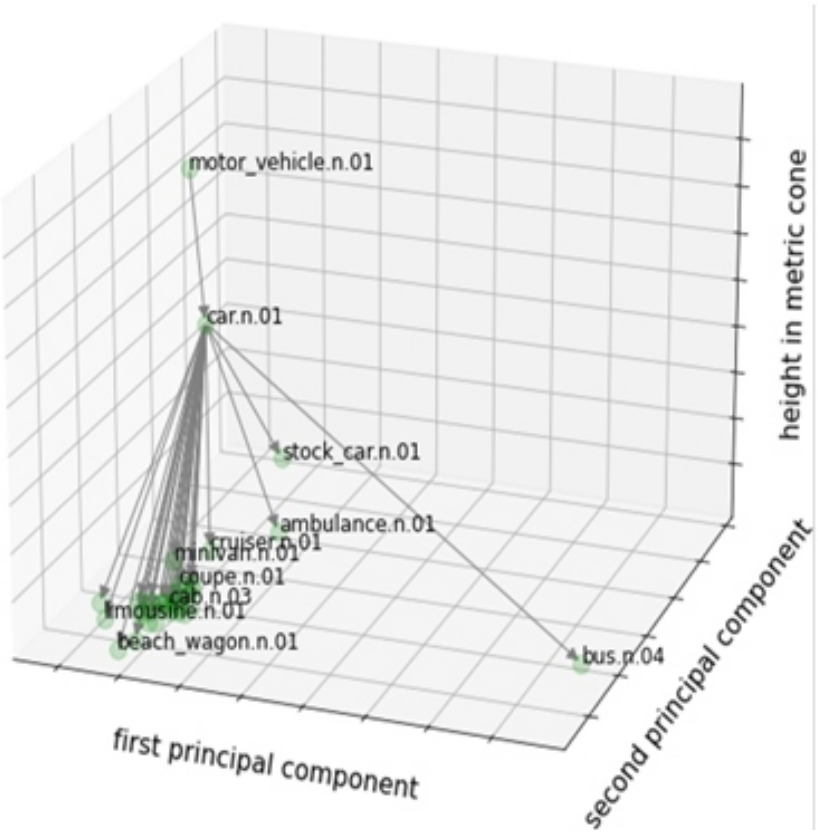

Figure 5. Visualization of wordnet hypernym and hyponym relations by cone embedding (beta: 1.0) learned from 10 to dimensional Euclidean embedding. The right figure is for the car and the left figure is for sport, describing the relationship with one higher or lower word. (In the visualization, all nodes are visualized, but only some of the word names corresponding to each node are shown. The original embedding vector (Euclidean in this case) is also made two-dimensional by PCA.)

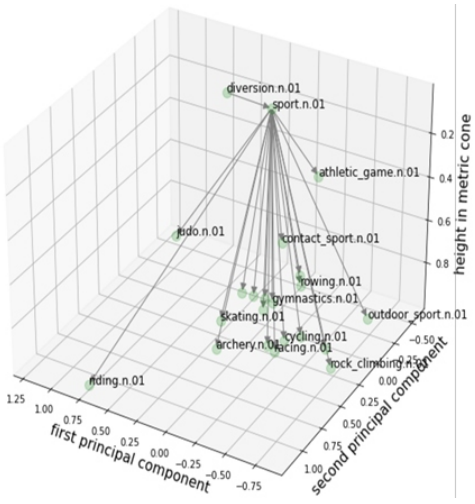

5. Discussion and Future Works

In this study, we have demonstrated that a graph embedding in a metric cone that is a dimension larger than the existing embedding methods has the following advantages: (1) we naturally define an index (score function) as an indicator of hierarchy, (2) the proposed method has some adaptivity since it can introduce the hierarchy into various pre-trained models by learning only newly added 1D parameters, and (3) thus, the optimization is computationally inexpensive and stable. By optimizing the 1D parameters, we have shown that the proposed method also has the flexibility to optimize the curvature to enhance the accuracy as well as other methods. Since the metric cone is defined as a space with +1 dimension with respect to the original metric space, it is also possible to learn cone embedding in the same way even when the original space is Poincaré. We demonstrated the feasibility of extracting the hierarchical structure using solely the additional space by fixing the original space and learning its embedding.

It is worth noting that an alternative approach involves directly embedding the graph into the metric cone by learning an embedding that includes the source space. However, the constraint of learning in one dimension offers some advantages. For instance, the metric cone is defined as a space with +1 dimension with respect to the original metric space, which allows for the learning of cone embedding in the same way for any general original spaces, including the Poincaré space. The independence of the optimization algorithm from the original embedding space results in a more stable computation. For example, the cone embedding performed best or fairly for overall settings while the Poincaré embedding performed very poorly in some experimental settings. Moreover, the tuning of hyperparameters such as β for embedding can be performed independently from the original embedding.

Author Contributions: Conceptualization, K.K.; Methodology, K.K.; Formal analysis, D.T.; Investigation, D.T.; Writing—original draft, D.T.; Writing—review & editing, K.K.; Supervision, K.K. All authors have read and agreed to the published version of the manuscript.

Funding: This work was supported by RIKEN AIP and JSPS KAKENHI (JP22K03439, JP19K00912).

Data Availability Statement: Tree-like graph data were randomly generated by the python library networkx (https://networkx.org/). WordNet (https://www.nltk.org/) was obtained from the python library NLTK (https://www.nltk.org/) and used for training. For the human numerical evaluation results used in the evaluation of the hierarchical scores, hyperlex (https://github.com/cambridgeltl/hyperlex) was used.

Acknowledgments: The idea of applying metric cones to data science was born during a collaboration with Henry P. Wynn.

Conflicts of Interest: The authors declare no conflict of interest.

Appendix A. Derivation of the Metric Tensor of a Metric Cone

Let $\mathcal{M}$ be an n-dimensional Riemannian manifold with a metric g. Then the metric $\bar{g}$ of the corresponding metric cone $\tilde{\mathcal{M}} = \tilde{\mathcal{M}}_\beta$ can be defined except the apex. Denote the square of the infinitesimal distance in $\tilde{\mathcal{M}}$ as $|d\bar{s}|^2$, then

$$\begin{aligned}
|d\bar{s}|^2 &= \bar{d}_\beta((x,r),(x+dx,r+dr))^2 \\
&= \beta^2\Big(2r^2 + 2rdr + dr^2 - 2(r+dr)r\cos(\pi\min(d_{\mathcal{M}}(x,x+dx)/\beta,1))\Big) \\
&\approx \beta^2\left(2r^2 + 2rdr + dr^2 - 2(r^2+rdr)\left(1 - \frac{(\pi d_{\mathcal{M}}(x,x+dx)/\beta)^2}{2}\right)\right) \\
&\approx \beta^2 dr^2 + \pi^2 r^2 \sum_{i,j} g_{ij}dx_i dx_j + \pi^2 r dr \sum_{i,j} g_{ij}dx_i dx_j \\
&= \begin{pmatrix} dx \\ dr \end{pmatrix}^\top \begin{pmatrix} (\pi^2 r^2 g_{ij}) & 0 \\ 0 & \beta^2 \end{pmatrix} \begin{pmatrix} dx \\ dr \end{pmatrix}. \qquad \text{(A1)}
\end{aligned}$$

Therefore, the metric tensor $\bar{g}$ becomes

$$\bar{g} = \begin{pmatrix} \pi^2 r^2 g & 0 \\ 0 & \beta^2 \end{pmatrix}. \qquad \text{(A2)}$$

Appendix B. Derivation of the Ricci and the Scalar Curvatures of a Metric Cone

We will derive the Ricci and scalar curvatures of metric cone $\tilde{\mathcal{M}}$ Let $0, 1, \ldots, n$ be the coordinate indices of metric cone $\tilde{\mathcal{M}}$ where 0 corresponds to the radial coordinate $s \in (0,1)$ and $1, \ldots, n$ correspond to $x \in \mathcal{M}$.

Claim A1. *The Ricci curvatures $\tilde{R}_{ij}$ and the scalar curvature $\tilde{R}$ become*

$$\tilde{R}_{\alpha\gamma} = R_{\alpha\gamma} - \pi^2(n-1)\beta^{-2}g_{\alpha\gamma}, \tilde{R}_{\alpha 0} = \tilde{R}_{0\alpha} = \tilde{R}_{00} = 0,$$

$$\tilde{R} = \{\pi^{-2}R - n(n-1)\beta^{-2}\}s^{-2} \qquad \text{(A3)}$$

where α and γ are coordinate indices in $1, \ldots, n$ and R_{ij} and R are the Ricci curvatures and the scalar curvature of $\mathcal{M}$, respectively.

Proof. By Example 4.6 of [32], if the metric of $\tilde{\mathcal{M}}$ is defined by the squared infinitesimal distance $|ds|^2$ in $\mathcal{M}$ and a $\mathcal{C}^2$-class function w on an open interval $J \subset \mathbb{R}$ as

$$|d\bar{s}|^2 = \beta^2|dr|^2 + w(r)^2|ds|^2, \qquad \text{(A4)}$$

the Ricci curvature tensor becomes

$$\tilde{R}_{\alpha\gamma} = R_{\alpha\gamma} - \left((n-1)\left(\frac{w'}{w}\right)^2 + \frac{w''}{w}\right)\tilde{g}_{\alpha\gamma} = R_{\alpha\gamma} - \left((n-1)\left(\frac{w'}{w}\right)^2 + \frac{w''}{w}\right)w^2 g_{\alpha\gamma},$$

$$\tilde{R}_{\alpha 0} = 0, \quad \tilde{R}_{00} = -(n-1)\frac{w''}{w} \tag{A5}$$

and the scalar curvature becomes

$$\tilde{R} = w^{-2}(R - n(n-1)(w')^2 - 2nww''). \tag{A6}$$

Since the metric of a metric cone $\bar{M}$ is given by

$$|d\bar{s}|^2 = \beta^2|dr|^2 + \pi^2 r^2|ds|^2, \tag{A7}$$

by setting $\tilde{r} := \beta r$ and $w(\tilde{r}) := \pi\beta^{-1}\tilde{r}$, we obtain the following form similar to (A4):

$$|d\bar{s}|^2 = |d\tilde{r}|^2 + w(\tilde{r})^2|ds|^2. \tag{A8}$$

By substituting $w(\tilde{r}) = \pi\beta^{-1}\tilde{r} = \pi r$, $w'(\tilde{r}) = \pi\beta^{-1}$ and $w''(\tilde{r}) = 0$, we obtain the Ricci and scalar curvatures in Claim A1. □

Appendix C. Identifiability of the Heights in the Cone Embedding

In this section, we will prove Theorem 1 of the main article. Let us begin by rewriting Theorem 1 as a longer but more theoretically rigorous form.

Theorem A1 (A rigorous restatement of Theorem 1). *Let Z be a length metric space and X be a metric cone of Z with a parameter $\beta > 0$. Let n be an integer at least 3. Fix $z_i \in Z$ and $x_i := (z_i, t_i) \in X$ with $t_i \in [0,1]$ for $i = 1, \ldots, n$. Denote a matrix $\tilde{D} := [\tilde{d}_\beta(x_i, x_j)]_{i,j=1}^n$.*

(a) Assume $z_1, \ldots, z_n$ are not all aligned in a geodesic. Given $z_1, \ldots, z_n$ and $\tilde{D}$, the number of possible values of $(t_1, \ldots, t_n)$ is at most four.

(b) Let $n \geq 4$ and assume $z_1, \ldots, z_n$ and $t_1, \ldots, t_n$ are in a "general" position. Here "general" position means that, besides the assumption in (a), given any four distinct points $z_i, z_j, z_k, z_l \in Z$ and corresponding heights $t_i, t_j, t_k \in [0,1]$, t_l can still take infinitely many values. Then $t_1, \ldots, t_n$ are determined uniquely by $z_1, \ldots, z_n$ and $\tilde{D}$.

(c) If $d(z_i, z_j) \geq \beta/2$ for all $i, j = 1, \ldots, n$, $i \neq j$, then $t_1, \ldots, t_n$ are determined uniquely by $z_1, \ldots, z_n$ and $\tilde{D}$.

Before the proof, we will state some remarks.

If $n = 2$, the identifiability problem reduces to an elementary geometric question: given a circle sector as the right two subfigures of Figure 1 of the main paper and the length of the blue line segment(s) connecting (x, s) and (y, t), can s and t be determined uniquely? The answer is evidently no. However, it is notable that there are two types of counterexamples. The first type is as Figure A1a, one point moves "up" and the other moves "down". The other type as Figure A1b is maybe counter-intuitive: both move "up" or "down". Note that the second case does not happen if the angle θ is larger than or equal to $\pi/2$.

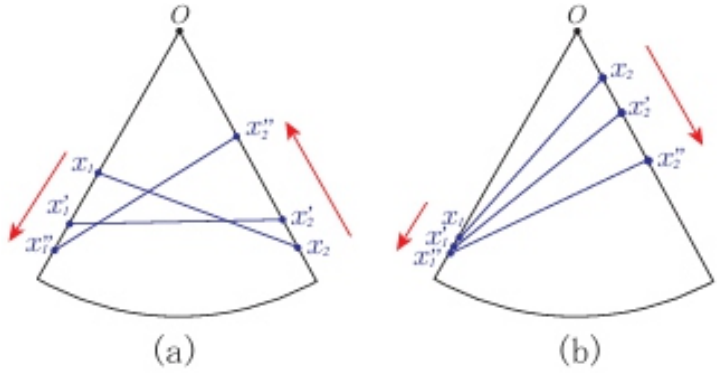

Figure A1. Two types of movement for a line segment of constant length (**a**) One point moves "up" and the other moves "down" (**b**) Both move "up" or "down".

If $n = 3$, the picture becomes a tetrahedron as in Figure A2. Here the angles and edge lengths are defined by

$$\begin{aligned} \theta_1 &:= \pi \min(d_Z(z_2, z_3)/\beta, 1), \quad a_1 := \tilde{d}_\beta(x_2, x_3) \\ \theta_2 &:= \pi \min(d_Z(z_3, z_1)/\beta, 1), \quad a_2 := \tilde{d}_\beta(x_3, x_1) \\ \theta_3 &:= \pi \min(d_Z(z_1, z_2)/\beta, 1), \quad a_3 := \tilde{d}_\beta(x_1, x_2) \end{aligned} \tag{A9}$$

and $\theta_1 + \theta_2 + \theta_3$ is assumed to be at most 2π. Then, the geometrical question becomes "when angles α, β, γ and edge lengths a_1, a_2, a_3 of triangle $\triangle x_1 x_2 x_3$ is given, can the position of the points x_1, x_2, and x_3 be determined uniquely?" If it is not unique and there are two different positions of x_1, x_2, and x_3, at least one edge should move as in Figure A1b since it is impossible to move all three edges as in Figure A1a. However, if all of the angles are larger than or equal to $\pi/2$, this cannot happen. This actually gives a geometrical proof of Theorem A1(c).

If $\theta_1 + \theta_2 + \theta_3$ is larger than 2π, the geometric arguments become complicated. We do not need this kind of case analysis when we use algebraic arguments as in the following proof.

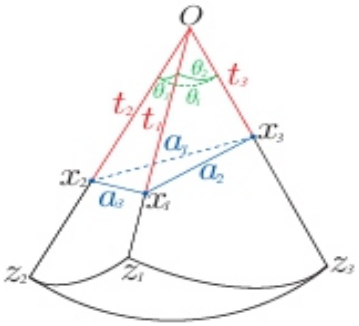

Figure A2. Metric cone generated by three points $z_1, z_2, z_3 \in Z$.

Now we will prove the theorem. In the proof, we use the Gröbner basis as a tool of computational algebra. See for example [33] about definition and application of the Gröbner basis.

Proof. (a) Since the maximum number of possible values of $(t_1, \ldots, t_n)$ does not increase with n, it is enough to prove for $n = 3$. We set $\theta_1, \theta_2, \theta_3 \in [0, \pi]$ and $a_1, a_2, a_3 \geq 0$ as (A9). Then, by the law of cosine,

$$
\begin{aligned}
t_2^2 + t_3^2 - 2t_2t_3\cos\theta_1 &= a_1^2,\\
t_3^2 + t_1^2 - 2t_3t_1\cos\theta_2 &= a_2^2,\\
t_1^2 + t_2^2 - 2t_1t_2\cos\theta_3 &= a_3^2.
\end{aligned} \tag{A10}
$$

We consider this as a system of polynomial equations with variables t_1, t_2, t_3 and compute the Gröbner basis of the ideal generated by the corresponding polynomials by degree lexicographic monomial order (deglex) with $t_1 > t_2 > t_3$ by Mathematica (see Note A1). Then the output becomes as in Note A1 and the basis includes $-t_1^2 + (2\cos\theta_2)t_1t_3 - t_3^2 + a_2^2$, $-t_2^2 + (2\cos\theta_3)t_2t_3 - t_3^2 + a_3^2$ and $4v(\theta_1,\theta_2,\theta_3)t_3^4 + (\text{terms of degree} \leq 2)$ where

$$
v(\theta_1,\theta_2,\theta_3) := 1 + 2\cos\theta_1\cos\theta_2\cos\theta_3 - \cos\theta_1^2 - \cos\theta_2^2 - \cos\theta_3^2. \tag{A11}
$$

Note that when $\theta_1 + \theta_2 + \theta_3 \leq 2\pi$, $\frac{a_1a_2a_3}{6}v(\theta_1,\theta_2,\theta_3)$ is a formula of the volume of the tetrahedron whose base triangle is $\triangle x_1x_2x_3$ and, therefore, it has a positive value unless the tetrahedron degenerates. By the assumption, z_1, z_2, z_3 are not aligned in a geodesic and therefore the tetrahedron does not degenerate and $v(\theta_1,\theta_2,\theta_3)$ must be nonzero. Note that this becomes negative when $\theta_1 + \theta_2 + \theta_3 > 2\pi$.

On the other hand, it is known that the system of polynomial equations with a Gröbner basis G has a finite number of (complex) solutions if and only if, for each variable x, G contains a polynomial with a leading monomial that is a power of x. Now, all variables t_1,t_2, and t_3 satisfy such a property; thus, we conclude there are at most a finite number of solutions.

Then, by Bézout's theorem, the number of solutions is at most the product of the degree of three polynomial equations, i.e., $2 \times 2 \times 2 = 8$. However, if (t_1, t_2, t_3) is a solution, $(-t_1, -t_2, -t_3)$ is also a solution, and only one of each pair can satisfy $t_1, t_2, t_3 \leq 0$. Thus, we conclude the number of possible values of (t_1, t_2, t_3) is at most four.

(b) By the assumptions in (a), without loss of generality, we can assume z_1, z_2, z_3 are not aligned in a geodesic. By the result of (a), given z_1, z_2, z_3 and distances $\bar{d}_\beta(x_1, x_2)$, $\bar{d}_\beta(x_1, x_3)$,$\bar{d}_\beta(x_2, x_3)$, there are at most four variations of the values of (t_1, t_2, t_3). Here we assume t_1 can take multiple values including $\hat{t}_1$ and $\check{t}_1$.

Suppose, in addition to the above, the values of z_4 and $d_\beta(x_1, x_4)(=: a_4)$ are given and let $\theta_4 := \pi\min(d_Z(z_1, z_4)/\beta, 1)$. Then, both $\hat{t}_1$ and $\check{t}_1$ satisfy $t_1^2 + t_4^2 - 2t_1t_4\cos\theta_4 = a_4^2$ and therefore $2t_4\cos\theta_4 = \hat{t}_1 + \check{t}_1$ must hold. Since $\hat{t}_1$ and $\check{t}_1$ are different non-negative values, $\hat{t}_1 + \check{t}_1 > 0$ and, therefore, $\cos\theta_4 \neq 0$. Hence, we obtain $t_4 = (\hat{t}_1 + \check{t}_1)/2\cos\theta$.

This means if t_4 takes values except $(\hat{t}_1 + \check{t}_1)/2\cos\theta$, at most only one of $\hat{t}_1$ and $\check{t}_1$ can be a solution. We can reduce each pairwise ambiguity of the (at most) four possibilities of (t_1, t_2, t_3) one by one similarly. Finally (t_1, t_2, t_3) are determined uniquely for all except at most $\binom{4}{2} = 6$ values of t_4. However, such finite values of t_4 can be neglected thanks to the assumption of the "general" position in the theorem. Since the same argument holds for any triplets, the statement has been proved.

(c) If $(t_1, \ldots, t_n)$ can take multiple values, without loss of generality we can assume (t_1, t_2, t_3) takes multiple values. By the assumption in the theorem, $\theta_1, \theta_2, \theta_3 \geq \pi/2$ and therefore all coefficients in each equation of (A10) become positive. Thus, if t_i increases/decreases then t_j must decrease/increase for $(i, j) = (1,2), (2,3), (3,1)$ but this cannot happen simultaneously. Hence, (t_1, t_2, t_3) cannot take multiple values.

Note that all of this proof works even when $\theta_1 + \theta_2 + \theta_3$ is larger than 2π. □

Remark A1. *The assumption in Theorem A1(a) is necessary. If the assumption fails, the tetrahedron degenerates and x_1, x_2, x_3 and the apex O are all in a plane. When O happens to be on a circle passing through x_1, x_2, and x_3, move O to another point O' on the same circle. Then, the angles corresponding to $\theta_1, \theta_2, \theta_3$ do not change by the inscribed angle theorem. By an elemental geometrical argument, a new position of x_1, x_2, x_3 and O' gives another solution of t_1, t_2, t_3. Hence, obviously, there are an infinite number of solutions.*

Remark A2. *The assumption of "general" positions of $z_1, \ldots, z_n$ in Theorem A1(b) is satisfied easily for most data distributions. For example, if both $z_1, \ldots, z_n \in \mathbb{R}^d$ and $t_1, \ldots, t_n \in [0, 1]$ are i.i.d. from a probability distribution whose density function exists with respect to the Lebesgue measure, then it is easy to see the assumption holds almost surely and therefore uniqueness of the solution is guaranteed. Note that, for $n = 3$ under the same setting, there can be multiple solutions with a positive probability.*

Note A1. *Computation of the Gröbner basis by Mathematica:*

For simplicity, we put $x := t_1$, $y := t_2$, $z := t_3$, $a := 2\cos\theta_1$, $b := 2\cos\theta_2$, $c := 2\cos\theta_3$, $d := a_1^2$, $e := a_2^2$, and $f := a_3^2$.

Note that the second, first, and last polynomials in the output correspond to $-t_1^2 + (2\cos\theta_2)t_1t_3 - t_3^2 + a_2^2$, $-t_2^2 + (2\cos\theta_3)t_2t_3 - t_3^2 + a_3^2$, and $4v(\theta_1, \theta_2, \theta_3)t_3^4 + (\text{terms of degree} \leq 2)$ in the proof, respectively.

```
------------------------------------------------------------
In := GroebnerBasis[{x^2 + y^2 - a*x*y - d, x^2 + z^2 - b*x*z - e,
y^2 + z^2 - c*y*z - f}, {x, y, z},
MonomialOrder -> DegreeLexicographic]

Out = {f - y^2 + c y z - z^2, e - x^2 + b x z - z^2,
d - x^2 + a x y - y^2,
d x - e x + a e y - x y^2 - b d z + b y^2 z + x z^2 -
a y z^2, -c d x + c e x - a c e y + b f y + c x y^2 - b y^3 +
b c d z - a f z + a y^2 z - c x z^2 - b y z^2 + a z^3,
a f x + d y - f y - x^2 y - c d z + c x^2 z - a x z^2 + y z^2,
b f x - c e y + c x^2 y - b x y^2 + e z - f z - x^2 z +
y^2 z, -c e x + a b f x + c x^3 + b d y - b f y - b x^2 y -
b c d z + a e z - a x^2 z + c x z^2 + b y z^2 - a z^3,
a c d x - a c e x + b f x + c d y - c e y + a^2 c e y - a b f y -
b x y^2 + a b y^3 - c y^3 - a b c d z + e z - f z + a^2 f z -
x^2 z + y^2 z - a^2 y^2 z + a c x z^2 + a b y z^2 -
a^2 z^3, -a e f - d x y + e x y + f x y + c d x z - c e x z +
b d y z - b f y z - b c d z^2 + a e z^2 + a f z^2 - 2 x y z^2 +
c x z^3 + b y z^3 - a z^4, -c d e + c e^2 - a b e f + c d x^2 -
c e x^2 - b d x y + b e x y + b f x y - a f x z - d y z +
b^2 d y z + 2 e y z + f y z - b^2 f y z - x^2 y z + 2 c d z^2 -
b^2 c d z^2 + a b e z^2 - 2 c e z^2 + a b f z^2 + a x z^3 -
3 y z^3 + b^2 y z^3 - a b z^4 + c z^4, -d x + a^2 d x + a b c d x +
2 e x - a^2 e x - a b c e x - a^2 f x + b^2 f x - x^3 + b c d y -
a e y + a^3 e y - b c e y + a^2 b c e y + a f y - a b^2 f y +
x y^2 - b^2 x y^2 - a y^3 + a b^2 y^3 - b c y^3 + b d z -
```

```
a^2 b d z + a c d z - a b^2 c d z + b e z - a c e z - b f z +
a^2 b f z - 2 x z^2 + 2 a^2 x z^2 - a^3 y z^2 + a b^2 y z^2 -
a^2 b z^3 + a c z^3, -c d^2 + c d e + a b d f + c d x^2 - c e x^2 +
b f x y - a b d y^2 + 2 c d y^2 - 2 c e y^2 + a^2 c e y^2 -
a b f y^2 - b x y^3 + a b y^4 - c y^4 - a d x z + a e x z -
a f x z - 2 d y z + e y z - a^2 e y z - f y z + a^2 f y z +
x^2 y z + 3 y^3 z - a^2 y^3 z,
d^2 - 2 d e + c^2 d e + e^2 - c^2 e^2 - 2 d f + b^2 d f + 2 e f -
a^2 e f + a b c e f + f^2 - b^2 f^2 - c^2 d x^2 + c^2 e x^2 +
b c d x y - b c e x y - b c f x y - b^2 d y^2 + b^2 f y^2 +
a c d x z - a c e x z + a c f x z + a b d y z + a b e y z -
a b f y z + 4 d z^2 - 2 b^2 d z^2 - a b c d z^2 - 2 c^2 d z^2 +
b^2 c^2 d z^2 - 4 e z^2 + a^2 e z^2 - a b c e z^2 + 2 c^2 e z^2 -
4 f z^2 + a^2 f z^2 + 2 b^2 f z^2 - a b c f z^2 + 4 z^4 - a^2 z^4 -
b^2 z^4 + a b c z^4 - c^2 z^4}
```

References

1. Zhang, J.; Ackerman, M.S.; Adamic, L. Expertise networks in online communities: Structure and algorithms. In Proceedings of the 16th international Conference on World Wide Web, Banff, AB, Canada, 8–12 May 2007; pp. 221–230.

2. DeChoudhury, M.; Counts, S.; Horvitz, E. Social media as a measurement tool of depression in populations. In Proceedings of the 5th Annual ACM WebScience Conference, Paris, France, 2–4 May 2013; pp. 47–56.

3. Page, L.; Brin, S.; Motwani, R.; Winograd, T. The PageRank Citation Ranking: Bringing Order to the Web; Technical Report; Stanford InfoLab, Stanford University: Stanford, CA, USA, 1999.

4. Barabasi, A.L.; Oltvai, Z.N. Network biology: Understanding the cell's functional organization. Nat. Rev. Genet. 2004, 5, 101–113. [CrossRef] [PubMed]

5. Yahya, M.; Berberich, K.; Elbassuoni, S.; Weikum, G. Robust question answering over the web of linked data. In Proceedings of the 22nd ACMInternational Conference on Information & Knowledge Management, San Francisco, CA, USA, 27 October–1 November 2013; pp. 1107–1116.

6. Hoffart, J.; Milchevski, D.; Weikum, G. STICS: Searching with strings, things, and cats. In Proceedings of the 37th International ACMSIGIRConference on Research & Development in Information Retrieval, Gold Coast, Queensland, Australia, 6–11 July 2014; pp. 1247–1248.

7. Klimovskaia, A.; Lopez-Paz, D.; Bottou, L.; Nickel, M. Poincaré maps for analyzing complex hierarchies in single-cell data. Nat. Commun. 2020, 11, 2966. [CrossRef] [PubMed]

8. Kipf, T.N.; Welling, M. Semi-supervised classification with graph convolutional networks. arXiv 2016, arXiv:1609.02907.

9. Ribeiro, L.F.; Saverese, P.H.; Figueiredo, D.R. struc2vec: Learning node representations from structural identity. In Proceedings of the 23rd ACM SIGKDDInternational Conference on Knowledge Discovery and Data Mining, Halifax, NS, Canada, 13–17 August 2017; pp. 385–394.

10. Hamilton, W.; Ying, Z.; Leskovec, J. Inductive representation learning on large graphs. Adv. Neural Inf. Process. Syst. 2017, 30, 1025–1035.

11. Goyal, P.; Ferrara, E. Graph embedding techniques, applications, and performance: A survey. Knowl. Based Syst. 2018, 151, 78–94. [CrossRef]

12. Grover, A.; Leskovec, J. node2vec: Scalable feature learning for networks. In Proceedings of the 22nd ACM SIGKDD International Conference on Knowledge Discovery and Data Mining, San Francisco, CA, USA, 13–17 August 2016; pp. 855–864.

13. Cao,S.; Lu, W.; Xu, Q. Grarep: Learning graph representations with global structural information. In Proceedings of the 24th ACMInternational on Conference on Information and Knowledge Management, Melbourne, VIC, Australia, 19–23 October 2015; pp. 891–900.

14. Tang, J.; Qu, M.; Wang, M.; Zhang, M.; Yan, J.; Mei, Q. Line: Large-scale information network embedding. In Proceedings of the 24th International Conference on World Wide Web, Florence, Italy, 18–22 May 2015; pp. 1067–1077.

15. Sun, Z.; Chen, M.; Hu, W.; Wang, C.; Dai, J.; Zhang, W. Knowledge Association with Hyperbolic Knowledge Graph Embeddings. In Proceedings of the 2020 Conference on Empirical Methods in Natural Language Processing (EMNLP), Association for Computational Linguistics, Online, 16–20 November 2020; pp. 5704–5716. [CrossRef]

16. Rezaabad, A.L.; Kalantari, R.; Vishwanath, S.; Zhou, M.; Tamir, J. Hyperbolic graph embedding with enhanced semi-implicit variational inference. In Proceedings of the International Conference on Artificial Intelligence and Statistics, PMLR, Virtual, 13–15 April 2021; pp. 3439–3447.

17. Nickel, M.; Kiela, D. Poincaré embeddings for learning hierarchical representations. In Proceedings of the Advances in Neural Information Processing Systems, Long Beach, CA, USA, 4–9 December 2017; pp. 6338–6347.

18. Zhang,Z.; Cai, J.; Zhang, Y.; Wang, J. Learning hierarchy-aware knowledge graph embeddings for link prediction. In Proceedings of the AAAI Conference on Artificial Intelligence, New York, NY, USA, 7–12 February 2020; Volume 34, pp. 3065–3072.

19. Chami, I.; Wolf, A.; Juan, D.C.; Sala, F.; Ravi, S.; Ré, C. Low-Dimensional Hyperbolic Knowledge Graph Embeddings. In Proceedings of the 58th Annual Meeting of the Association for Computational Linguistics, Association for Computational Linguistics, Online, 5–10 July 2020; pp. 6901–6914. [CrossRef]

20. Dhingra, B.; Shallue, C.; Norouzi, M.; Dai, A.; Dahl, G. Embedding Text in Hyperbolic Spaces. In Proceedings of the Twelfth Workshop on Graph-Based Methods for Natural Language Processing (TextGraphs-12),Association for Computational Linguistics, NewOrleans, LA, USA, 6 June 2018; pp. 59–69. [CrossRef]

21. Nickel, M.; Kiela, D. Learning Continuous Hierarchies in the Lorentz Model of Hyperbolic Geometry. In Proceedings of the Machine Learning Research, PMLR, Stockholmsmässan, Stockholm, Sweden, 10–15 July 2018; Volume 80, pp. 3779–3788.

22. Ganea, O.; Becigneul, G.; Hofmann, T. Hyperbolic Entailment Cones for Learning Hierarchical Embeddings. In Proceedings of the Machine Learning Research, PMLR, Stockholmsmässan, Stockholm, Sweden, 10–15 July 2018; Volume 80, pp. 1646–1655.

23. Sala, F.; De Sa, C.; Gu, A.; Ré, C. Representation tradeoffs for hyperbolic embeddings. In Proceedings of the International Conference on Machine Learning, PMLR, Stockholm, Sweden, 10–15 July 2018; pp. 4460–4469.

24. Kobayashi, K.; Wynn, H.P. Empirical geodesic graphs and CAT (k) metrics for data analysis. Stat. Comput. 2020, 30, 1–18. [CrossRef]

25. Wilson, R.C.; Hancock, E.R.; Pekalska, E.; Duin, R.P. Spherical and Hyperbolic Embeddings of Data. IEEE Trans. Pattern Anal. Mach. Intell. 2014, 36, 2255–2269. [CrossRef] [PubMed]

26. Chami,I.; Ying, Z.; Ré, C.; Leskovec, J. Hyperbolic Graph Convolutional Neural Networks. In Proceedings of the Advances in Neural Information Processing Systems; Wallach, H., Larochelle, H., Beygelzimer, A., d'Alché-Buc, F., Fox, E., Garnett, R., Eds.; Curran Associates, Inc.: Red Hook, NY, USA, 2019; Volume 32.

27. Sturm, K.T. Probability measures on metric spaces of nonpositive curvature. In Proceedings of the Heat Kernels and Analysis on Manifolds, Graphs, and Metric Spaces: Lecture Notes A Quart, Program Heat Kernels, Random Walks, Analysis Manifolds Graphs, Emile Borel Cent. Henri Poincaré Institute, Paris, France, 16 April–13 July 2002 ; Volume 338, p. 357. Available online: https://bookstore.ams.org/conm-338 (accessed on 24 February 2023).

28. Deza, M.M.; Deza, E. Encyclopedia of Distances; Springer: Berlin/Heidelberg, Germany, 2009; pp. 1–583. 29. Loustau, B. Hyperbolic geometry. arXiv 2020, arXiv:2003.11180.

30. Sarkar, R. Low distortion delaunay embedding of trees in hyperbolic plane. In Proceedings of the International Symposium on Graph Drawing, Eindhoven, The Netherlands, 21–23 September 2011; pp. 355–366.

31. Barabasi, A.L.; Albert, R. Emergence of Scaling in Random Networks. Science 1999, 286, 509–512. [CrossRef] [PubMed]

32. Janson, S. Riemannian geometry: Some examples, including map projections. Notes. 2015. Available online: http://www2.math. uu.se/~svante/papers/sjN15.pdf (accessed on 24 February 2023).

. 33. Cox,D.; Little, J.; OShea, D. Ideals, Varieties, and Algorithms: An Introduction to Computational Algebraic Geometry and Commutative Algebra; Springer Science & Business Media: Berlin/Heidelberg, Germany, 2013.

Instructions for Authors

Essentials for Publishing in this Journal

1 Submitted articles should not have been previously published or be currently under consideration for publication elsewhere.

2 Conference papers may only be submitted if the paper has been completely re-written (taken to mean more than 50%) and the author has cleared any necessary permission with the copyright owner if it has been previously copyrighted.

3 All our articles are refereed through a double-blind process.

4 All authors must declare they have read and agreed to the content of the submitted article and must sign a declaration correspond to the originality of the article.

Submission Process

All articles for this journal must be submitted using our online submissions system. http://enrichedpub.com/ . Please use the Submit Your Article link in the Author Service area.

Manuscript Guidelines

The instructions to authors about the article preparation for publication in the Manuscripts are submitted online, through the e-Ur (Electronic editing) system, developed by **Enriched Publications Pvt. Ltd**. The article should contain the abstract with keywords, introduction, body, conclusion, references and the summary in English language (without heading and subheading enumeration). The article length should not exceed 16 pages of A4 paper format.

Title

The title should be informative. It is in both Journal's and author's best interest to use terms suitable. For indexing and word search. If there are no such terms in the title, the author is strongly advised to add a subtitle. The title should be given in English as well. The titles precede the abstract and the summary in an appropriate language.

Letterhead Title

The letterhead title is given at a top of each page for easier identification of article copies in an Electronic form in particular. It contains the author's surname and first name initial .article title, journal title and collation (year, volume, and issue, first and last page). The journal and article titles can be given in a shortened form.

Author's Name

Full name(s) of author(s) should be used. It is advisable to give the middle initial. Names are given in their original form.

Contact Details

The postal address or the e-mail address of the author (usually of the first one if there are more Authors) is given in the footnote at the bottom of the first page.

Type of Articles

Classification of articles is a duty of the editorial staff and is of special importance. Referees and the members of the editorial staff, or section editors, can propose a category, but the editor-in-chief has the sole responsibility for their classification. Journal articles are classified as follows:

Scientific articles:

1. Original scientific paper (giving the previously unpublished results of the author's own research based on management methods).

2. Survey paper (giving an original, detailed and critical view of a research problem or an area to which the author has made a contribution visible through his self-citation);

3. Short or preliminary communication (original management paper of full format but of a smaller extent or of a preliminary character);

4. Scientific critique or forum (discussion on a particular scientific topic, based exclusively on management argumentation) and commentaries. Exceptionally, in particular areas, a scientific paper in the Journal can be in a form of a monograph or a critical edition of scientific data (historical, archival, lexicographic, bibliographic, data survey, etc.) which were unknown or hardly accessible for scientific research.

Professional articles:

1. Professional paper (contribution offering experience useful for improvement of professional practice but not necessarily based on scientific methods);
2. Informative contribution (editorial, commentary, etc.);
3. Review (of a book, software, case study, scientific event, etc.)

Language

The article should be in English. The grammar and style of the article should be of good quality. The systematized text should be without abbreviations (except standard ones). All measurements must be in SI units. The sequence of formulae is denoted in Arabic numerals in parentheses on the right-hand side.

Abstract and Summary

An abstract is a concise informative presentation of the article content for fast and accurate Evaluation of its relevance. It is both in the Editorial Office's and the author's best interest for an abstract to contain terms often used for indexing and article search. The abstract describes the purpose of the study and the methods, outlines the findings and state the conclusions. A 100- to 250-Word abstract should be placed between the title and the keywords with the body text to follow. Besides an abstract are advised to have a summary in English, at the end of the article, after the Reference list. The summary should be structured and long up to 1/10 of the article length (it is more extensive than the abstract).

Keywords

Keywords are terms or phrases showing adequately the article content for indexing and search purposes. They should be allocated heaving in mind widely accepted international sources (index, dictionary or thesaurus), such as the Web of Science keyword list for science in general. The higher their usage frequency is the better. Up to 10 keywords immediately follow the abstract and the summary, in respective languages.

Acknowledgements

The name and the number of the project or programmed within which the article was realized is given in a separate note at the bottom of the first page together with the name of the institution which financially supported the project or programmed.

Tables and Illustrations

All the captions should be in the original language as well as in English, together with the texts in illustrations if possible. Tables are typed in the same style as the text and are denoted by numerals at the top. Photographs and drawings, placed appropriately in the text, should be clear, precise and suitable for reproduction. Drawings should be created in Word or Corel.

Citation in the Text

Citation in the text must be uniform. When citing references in the text, use the reference number set in square brackets from the Reference list at the end of the article.

Footnotes

Footnotes are given at the bottom of the page with the text they refer to. They can contain less relevant details, additional explanations or used sources (e.g. scientific material, manuals). They cannot replace the cited literature.
The article should be accompanied with a cover letter with the information about the author(s): surname, middle initial, first name, and citizen personal number, rank, title, e-mail address, and affiliation address, home address including municipality, phone number in the office and at home (or a mobile phone number). The cover letter should state the type of the article and tell which illustrations are original and which are not.